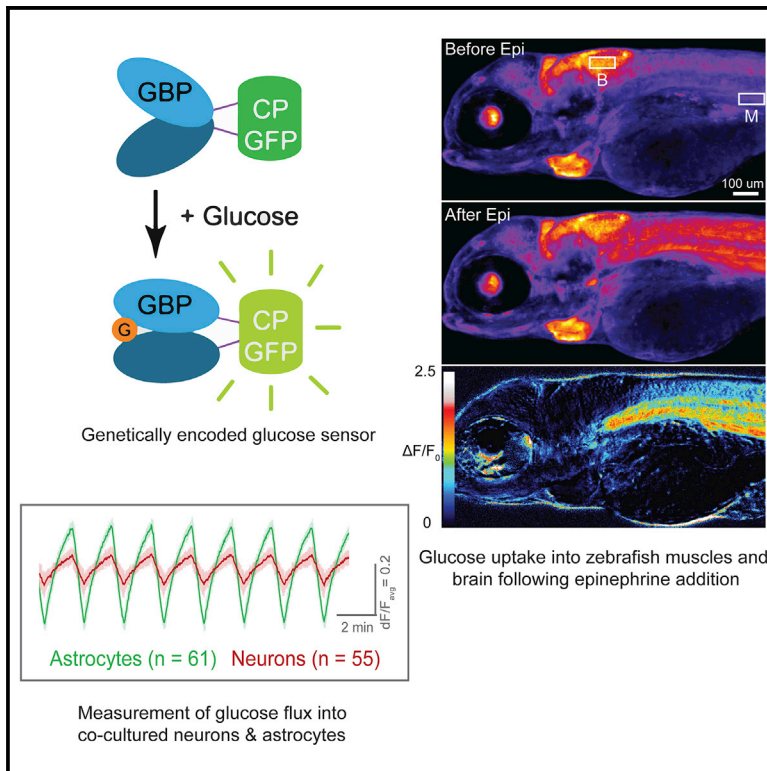


# *In vivo* glucose imaging in multiple model organisms with an engineered single-wavelength sensor

## Graphical abstract



## Authors

Jacob P. Keller, Jonathan S. Marvin, Haluk Lacin, ..., Minoru Koyama, Philipp J. Keller, Loren L. Looger

## Correspondence

[jacob.keller@usuhs.edu](mailto:jacob.keller@usuhs.edu) (J.P.K.), [loogerl@hhmi.org](mailto:loogerl@hhmi.org) (L.L.L.)

## In brief

Keller et al. describe a glucose-specific single-wavelength genetically encoded fluorescent sensor with a high signal-to-noise ratio and fast kinetics. They use it to follow glucose transport in neuron/astrocyte co-culture and in intact *Drosophila* central nervous system explants. It also reports glucose responses to pharmacological manipulations in live zebrafish embryos.

## Highlights

- An engineered sensor can detect glucose in living animals with a good signal-to-noise ratio
- The sensor can be used to screen molecules that modulate glucose transporter function
- The sensor reveals a rostral-caudal glucose transport pathway in fly larval CNS
- Two-color imaging shows effects of drugs on glucose transport in living zebrafish



## Resource

# *In vivo* glucose imaging in multiple model organisms with an engineered single-wavelength sensor

Jacob P. Keller,<sup>1,4,\*</sup> Jonathan S. Marvin,<sup>1</sup> Haluk Lacin,<sup>1,5</sup> William C. Lemon,<sup>1</sup> Jamien Shea,<sup>1,6</sup> Soomin Kim,<sup>2,7</sup> Richard T. Lee,<sup>2,3</sup> Minoru Koyama,<sup>1,8</sup> Philipp J. Keller,<sup>1</sup> and Loren L. Looger<sup>1,9,\*</sup>

<sup>1</sup>Janelia Research Campus, Howard Hughes Medical Institute, Ashburn, VA, USA

<sup>2</sup>Harvard Department of Stem Cell and Regenerative Biology, Harvard Stem Cell Institute, Harvard Medical School, Brigham and Women's Hospital, Cambridge, MA, USA

<sup>3</sup>The Cardiovascular Division, Department of Medicine, Harvard Medical School, Brigham and Women's Hospital, Cambridge, MA, USA

<sup>4</sup>Present address: Uniformed Services University of the Health Sciences, Bethesda, MD, USA

<sup>5</sup>Present address: Department of Genetics, Washington University School of Medicine, St. Louis, MO, USA

<sup>6</sup>Present address: Department of Neurobiology & Behavior, Cornell University, Ithaca, NY, USA

<sup>7</sup>Present address: Kaiser Permanente, Los Angeles, CA, USA

<sup>8</sup>Present address: Department of Cell & Systems Biology, University of Toronto, Toronto, ON, Canada

<sup>9</sup>Lead contact

\*Correspondence: [jacob.keller@usuhs.edu](mailto:jacob.keller@usuhs.edu) (J.P.K.), [loogerl@hhmi.org](mailto:loogerl@hhmi.org) (L.L.L.)

<https://doi.org/10.1016/j.celrep.2021.109284>

## SUMMARY

Glucose is arguably the most important molecule in metabolism, and its dysregulation underlies diabetes. We describe a family of single-wavelength genetically encoded glucose sensors with a high signal-to-noise ratio, fast kinetics, and affinities varying over four orders of magnitude (1  $\mu$ M to 10 mM). The sensors allow mechanistic characterization of glucose transporters expressed in cultured cells with high spatial and temporal resolution. Imaging of neuron/glia co-cultures revealed  $\sim$ 3-fold faster glucose changes in astrocytes. In larval *Drosophila* central nervous system explants, intracellular neuronal glucose fluxes suggested a rostro-caudal transport pathway in the ventral nerve cord neuropil. In zebrafish, expected glucose-related physiological sequelae of insulin and epinephrine treatments were directly visualized. Additionally, spontaneous muscle twitches induced glucose uptake in muscle, and sensory and pharmacological perturbations produced large changes in the brain. These sensors will enable rapid, high-resolution imaging of glucose influx, efflux, and metabolism in behaving animals.

## INTRODUCTION

D-glucose is a central molecule of energy metabolism. It is a preferred source of energy for most bacteria (Jahreis et al., 2008) and fungi, the photosynthetic product of plants, and the primary circulating energy source in animals. Glucose dysregulation is the hallmark of diabetes, and it is central to obesity and metabolic syndrome (Kaur, 2014). Taken together, these conditions contribute to a burgeoning global health crisis, and they exacerbate most other health problems, including cancer (Braun et al., 2011) and heart disease (Low Wang et al., 2016). Tools to monitor glucose are thus of paramount importance to both clinical diagnoses and basic science. In the brain, there are many mysteries surrounding glucose in particular and bioenergetics in general. Glucose is the primary energy source of the brain, but in what cells does glucose metabolism occur? Do glycolysis and oxidative phosphorylation (Ashrafi and Ryan, 2017) occur in the same cells? Do neurons in fact utilize glucose directly or is it first converted to lactate by the proposed astrocyte-neuron lactate shuttle (Magistretti and Allaman, 2015)? Do

synaptic terminals rely on local glycolysis to support energy-intensive processes (Rangaraju et al., 2014)? What are the roles of specific glucose transporters (Ashrafi et al., 2017), e.g., Glut1, Glut3, and Glut4, in neuronal and glial glucose uptake?

To address these and other critical questions, tools that can specifically detect glucose are required. The most useful tools will satisfy the following criteria: they should (1) be easily targetable to specific cell types, sub-cellular compartments, and organelles, and even to specific proteins of interest such as glucose transporters; (2) be genetically encoded (i.e., protein-based) to enable generation of viruses and transgenic animals (and the above targetability); (3) be soluble proteins (as opposed to integral membrane proteins) to provide maximal flexibility in targeting, such as to the cytoplasm or inside specific organelles; (4) be compatible with long-term imaging, and stable over time, to facilitate longitudinal studies; (5) not require any cofactors, other added molecules, or endogenous molecules of non-uniform distribution; (6) provide for cellular and sub-cellular resolution detection; (7) respond roughly as quickly as the underlying phenomena; (8) not perturb physiological phenomena being



measured; and (9) ideally be amenable to straightforward detection without sophisticated equipment.

Techniques for glucose monitoring in fluids (blood, urine), mainly to assist diabetic patients in maintaining euglycemia, have existed for decades and have gone through multiple cycles of optimization (Wang and Lee, 2015). Current methods for *ex vivo* glucose monitoring, however, are incompatible with the demands for *in vivo* detection listed above. The dominant technology for *ex vivo* glucose monitoring is indirect detection of glucose levels through electrochemical detection of H<sub>2</sub>O<sub>2</sub> release from glucose breakdown by the enzyme glucose oxidase (Guilbault and Lubrano, 1973). This technique is sensitive and rapid, but it reports from only single sites (Weltin et al., 2016) and lacks cellular resolution and targetability. Historically, the primary method of *in vivo* glucose tracking (usually used as a proxy for metabolic activity) is systemic injection of the non-metabolizable, radiolabeled glucose analog 2-[F<sup>18</sup>]fluoro-2-deoxy-D-glucose (FDG), whose accumulation is imaged by position emission tomography (PET) (Phelps et al., 1979). FDG, however, is not targetable, PET's spatial resolution is fundamentally limited to several millimeters (Moses, 2011), and each scan takes from 10s of seconds to minutes. Since FDG is not metabolized, it has dramatically different pharmacokinetics from glucose, and as such is only an approximation of initial glucose uptake, and may affect glucose trafficking itself. Thus, it is clear that these methods do not fit the criteria mentioned above, and better methods for *in vivo* glucose monitoring are required.

Fluorescence microscopy has revolutionized the study of physiology, allowing high spatiotemporal resolution of signaling events in intact animals and plants. The use of genetically encoded indicators further allows imaging to be targeted to specific cell types of interest and even to sub-cellular compartments; stable expression through transgenics, viral transduction, and other methods allows longitudinal experiments up to years. The first fluorescent glucose sensors were developed from the plant lectin concanavalin A (Schultz et al., 1982). These sensors, however, required *in vitro* derivatization with small-molecule dyes and injection, and fluorescence changes were either poor (*in vitro*) or unmeasurable (plasma) (McCartney et al., 2001). Specificity was also lacking, since concanavalin A also binds to other sugars and glycans (Mandal et al., 1994).

The cloning of bacterial periplasmic glucose-binding proteins (GBPs) has led to a wide array of sensing modalities. The introduction of single cysteine residues allows coupling of thiol-reactive small-molecule fluorophores that respond to glucose binding with alterations in fluorescence intensity, lifetime, emission wavelength, or fluorescence resonance energy transfer (FRET) ratios (Ge et al., 2004; Marvin and Hellinga, 1998; Tolosa et al., 1999), but such sensors would require injection into living specimens, with unknown targeting and poor *in vivo* stability. The first fully genetically encoded fluorescent glucose sensor resulted from the fusion of cyan and yellow fluorescent proteins (CFP, YFP) to the termini of *Escherichia coli* glucose/galactose-binding protein (GGBP) (Fehr et al., 2003). These initial sensors showed modest response amplitudes (<10% change in FRET between CFP and YFP), but they allowed imaging of glucose influx into cultured mammalian cells. Iterative structure-based modification of these sensors optimized the dissoci-

ation constant (K<sub>D</sub>) and increased FRET change to ~60% (Deuschle et al., 2005; Takanaga et al., 2008), which facilitated experiments such as identification of the SWEET family of glucose transporters mediating pollen viability and bacterial virulence, among other functions (Chen et al., 2010), and glucose signaling in rice roots in response to diverse stressors (Zhu et al., 2017). FRET, however, has fundamental limitations (Leavesley and Rich, 2016; Piston and Kremers, 2007), primarily a low signal-to-noise ratio (SNR), particularly with the sensitized emission modality, which requires image processing to remove donor-acceptor crosstalk and convolves together noise from both labels. Furthermore, analysis can be confounded unpredictably by different rates of photobleaching and pH sensitivities of the constituent probes. Accordingly, despite the advances in this family of indicators and its successes (Miyamoto and Amrein, 2019; Piquet et al., 2018; Volkenhoff et al., 2018), the modest fluorescence responses have hampered widespread application to challenging preparations such as living animals.

Our lab has recently developed a technique for engineering single-wavelength indicators from circularly permuted green fluorescent protein (cpGFP) and periplasmic binding proteins for a variety of small molecules, including glutamate (Marvin et al., 2013, 2018), gamma-aminobutyric acid (GABA) (Marvin et al., 2019), maltose (Marvin et al., 2011), phosphonates (Alicea et al., 2011), and acetylcholine (Borden et al., 2020), among others. Another group has also used this technique to develop sensors for histidine (Hu et al., 2017) and recently glucose (sensor "FGBP" made using *E. coli* GGBP) (Hu et al., 2018). FGBP, based on YFP, was specific for D-glucose and D-galactose over other sugars tested, and it produced a ~200% change in the fluorescence excitation ratio in *E. coli* cells upon addition of glucose. However, the FGBP sensor was not tested in any other preparation.

Herein, we present a series of genetically encoded green glucose sensors with a high signal-to-noise ratio, rapid kinetics, and simple imaging. We also demonstrate use of these sensors in a number of applications: characterization of glucose transporter function and inhibitor properties, separate visualization of neuronal and glial metabolic rates in co-culture, discovery of a putative glucose transport pathway in fruit fly central nervous system, and tracking of glucose transport in the muscles and brains of living larval zebrafish. These sensors will facilitate longitudinal glucose imaging studies in living animals and plants, with high spatial and temporal resolution.

## RESULTS

### Sensor engineering and protein characterization

A survey of the Protein Data Bank revealed several structures of GBPs from multiple organisms, including mesophiles *E. coli*, *Pseudomonas putida*, *Yersinia pestis*, *Salmonella typhimurium*, and *Chloroflexus aurantiacus*, and hyperthermophiles *Thermus thermophilus* and *Thermotoga maritima*. Because proteins from thermophiles often exhibit enhanced stability, the GBP from the thermophile *T. thermophilus* was selected as the scaffold. It also has high structural similarity (Cuneo et al., 2006) to *E. coli* maltose-binding protein, from which we previously made a sensor (Marvin et al., 2011), thus facilitating engineering.

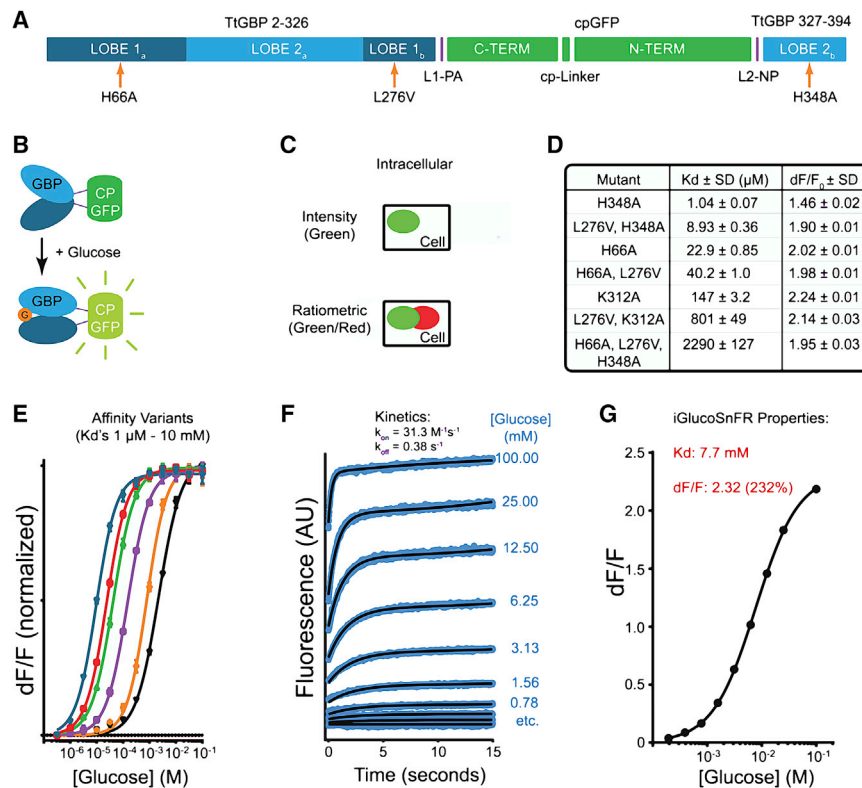


**Figure 1. Sensor design and properties**

(A) Schematic of iGlucoSnFR sensor sequence. Circularly permuted green fluorescent protein (cpGFP, green) was inserted into glucose-binding protein (GBP, light and dark blue) from *T. thermophilus*. Affinity-lowering mutations are indicated (orange arrows). “LOBEs” refer to the two subdomains on opposing sides of the ligand-binding pocket of GBP.

(B) Schematic of iGlucoSnFR sensor construction. cpGFP (green) was inserted into GBP (light and dark blue) from *T. thermophilus* such that binding of glucose (G, orange disk) to GBP induced fluorescence increases in cpGFP.

(C) Sensor architecture. Sensors were made with the addition of a glucose-insensitive red fluorescent protein mRuby2 to allow for ratiometric measurements and/or cell typing. Sensors are shown schematically as green ellipses; mRuby2 is shown as red ellipses.

(D and E) Affinity variants. Permutations of binding site residue mutations (H66A, L276V, K312A, H348A) yielded iGlucoSnFR variants with affinities spanning the range of 1  $\mu\text{M}$  to 10 mM when measured in PBS. Each curve in (E) represents a sensor with different affinity, with fluorescence changes normalized by lowest and highest values. The last entry in (D) (H66A, L276V, H348A) and the rightmost curve in (E) represent iGlucoSnFR as used in the rest of the text. Values are mean  $\pm$  SD of  $n = 3$  experimental replicates.

(F) iGlucoSnFR kinetics. Stopped-flow fluorescence measurements on the final construct were

performed at several concentrations, and kinetic rate constants were fit to data. Values are mean  $\pm$  SD of  $n = 5$  experimental replicates.

(G) Final iGlucoSnFR binding curve, constructed from the data in (F). Sensor parameters are as shown. Note that these data were collected at pH 8.2 to increase  $\Delta F/F$  for kinetics accuracy, thus increasing the  $K_D$  relative to neutral pH. Error bars (SD) are plotted, but they are hidden by the symbols. Values are mean  $\pm$  SD of  $n = 3$  experimental replicates.

A gene encoding *T. thermophilus* GBP lacking the periplasmic secretion leader peptide (amino acids 1–26) was synthesized and cloned into bacterial expression vector pRSET-A (Invitrogen). Based on homology to the maltose sensor, GlyGly-cpGFP-GlyGly was inserted between residues 326 and 327 of TiGBP (Figures 1A and 1B). To reduce glucose affinity for screening purposes and tune affinity for measuring physiologically relevant levels of glucose, residues His66 and His348, which form aromatic stacking interactions with bound glucose, as well as Lys312, which forms hydrogen bonds, were mutated to alanine. Leu276, which packs against the glucose, was mutated to valine. Both GlyGly linkers were randomized by targeted mutagenesis, and variants were screened for changes in fluorescence upon addition of saturating glucose. A variant, Linker1-ProAla/Linker2-AsnPro (L1-PA/L2-NP), was identified with a fluorescence response ( $\Delta F/F$ ) of 1.95 and  $K_D$  for glucose of 2.3 mM when measured in phosphate-buffered saline (PBS) at pH 7.4 (Figure 1D). We refer to this sensor as intensity-based glucose-sensing fluorescent reporter (iGlucoSnFR; not to be confused with our other sensor iGluSnFR, which responds to glutamate). We tested the binding of iGlucoSnFR to a range of other sugars (Figure S1A); only D-galactose and 2-deoxyglucose responded, but with weaker affinity ( $K_D = 20$  and 45 mM, respectively) and lower  $\Delta F/F$  (1.6 and 0.52, respectively), iGlucoSnFR responded to glucose across a range of pH values

from 6.0 to 9.5 (Figure S1B), with  $K_D$  and  $\Delta F/F$  both trending to higher values with increased pH.

For use in eukaryotic cells, we cloned iGlucoSnFR, without the N-terminal affinity purification sequence from pRSET-A, into a cytomegalovirus (CMV) promoter-containing vector derived from pDisplay (Invitrogen) for cytoplasmic expression (Figure 1G). We also tagged the C terminus with the red fluorescent protein mRuby2 (Lam et al., 2012) to control for expression and movement artifacts (Figures S1C, S1D, and S2). Additionally, combinations of four different binding site mutations (H66A, L276V, K312A, H348A) were tested to produce an affinity series of six sensors spanning four orders of magnitude (Figures 1D and 1E). Stopped-flow fluorescence showed relatively rapid rates of signal increase upon binding glucose ( $k_{on} = 31 \text{ M}^{-1}\text{s}^{-1}$ ) and signal decrease upon glucose unbinding ( $k_{off} = 0.38 \text{ s}^{-1}$ ) (Figure 1F). The average of the rate constants ( $n = 5$  replicates) at each [Glc] was used to determine a steady-state binding isotherm (Figure 1G).

### Imaging glucose transporter activity

We have previously demonstrated the utility of cytoplasmic sensors to report the activity of membrane transporters in cultured cells with excellent spatial (sub-cellular) and temporal (milliseconds) resolution (Keller and Looger, 2016). HEK293T cells were co-transfected with plasmids encoding cytoplasmic iGlucoSnFR

with or without the human glucose uniporter Glut1/SLC2A1 (Mueckler et al., 1985). Buffers alternating between 0 and 20 mM glucose (substituted with equimolar sorbitol to maintain constant osmolarity) (Figure 2A) were perfused continuously onto cells, with a periodicity of 60 s. Corresponding fluorescence changes were imaged on an inverted Zeiss LSM 800 confocal microscope at 2 Hz;  $\sim 10$  oscillation periods were measured to establish baseline oscillation magnitudes and variability. Cells without Glut1 co-transfection responded negligibly to this stimulus, whereas those expressing Glut1 displayed marked oscillations in fluorescence intensity. The Glut1 inhibitor cytochalasin B (CCB, a competitive inhibitor) was then superadded to these buffers at varying concentrations. CCB reversibly decreased Glut1 transport activity in a dose-dependent manner (Figure 2B). CCB binds to the intracellular side of Glut1 (Kapoor et al., 2016) and thus must enter the cell before it can act. Consistent with that mechanism, steady-state inhibition was achieved after about two oscillation periods ( $\sim 120$  s) at each concentration. Once steady-state inhibition was achieved, magnitudes were quantified relative to baseline, and a half-maximal inhibitory concentration ( $IC_{50}$ ) of  $\sim 0.6$   $\mu$ M was fit to these data, consistent with literature values (Kapoor et al., 2016).

### Characterization of glucose dynamics in neuronal/glia co-cultures

Next, we measured intracellular responses of co-cultured rat astrocytes and neurons to physiological levels of glucose. Adeno-associated viruses (AAVs) were used to express iGlucoSnFR and iGlucoSnFR-mRuby2 under promoters specific for neurons (*hSynapsin-1*) or astrocytes (*gfaABC<sub>1</sub>D*). Cultures were co-infected with AAV2/1-*hSynapsin-1*-iGlucoSnFR-mRuby2 and AAV2/1-*gfaABC<sub>1</sub>D*-iGlucoSnFR, thus labeling both cell types with the glucose sensor and neurons with an additional red fluorescent protein (Figure 2C). These cultures were subjected to continuously perfused buffers alternating between 0 and 20 mM glucose with a total period of 2 min, with relative times in each buffer adjusted to preserve approximate linearity in fluorescence response waveforms (80 s with glucose, 40 s without). Constant confocal imaging in both green and red channels (Figure 2D; Data S1) revealed  $\sim 3$ -fold larger fluorescence oscillations in astrocytes compared to neurons (Figures 2E–2G). Oscillation magnitudes were nearly identical regardless of which cell type expressed the mRuby2-fused sensor (Figure S3). Although the cell body-free background (Figure 2E1) appears to have significant oscillation amplitude, close inspection reveals that this background is a dense network of cellular processes that are enhanced by fast Fourier transform (FFT) processing and the  $\Delta F/F_{avg}$  calculation. The oscillation patterns of these processes correlate better with the green-only (astrocytic) fluorescence signal (Figure 2D1) than with the green + red (neuronal) signal (Figure 2D2), and astrocyte cell bodies have roughly similar amplitudes as the processes' amplitudes, indicating that the processes are likely astrocytic. In this experiment, red fluorescence intensity correlated inversely with oscillation magnitude, providing a holistic picture of the relative indifference of neurons to glucose in comparison to that of astrocytes (compare Figure 2E1 with Figure 2E2; correlation is plotted in Figure 2F).

Although metabolic consumption of glucose contributes modestly to these fluorescence changes (Bittner et al., 2010), the magnitude of observed fluorescence changes indicates significantly larger glucose transport in astrocytes compared to neurons under these *in vitro* conditions, consistent with some previous results (Hara et al., 1989) but in conflict with others (Lundgaard et al., 2015). (See Supplemental materials and methods for a discussion of transport versus metabolism estimations.) It is possible in the latter case that the absence of transport blockers in wash solutions allowed radiolabeled glucose analogs to escape prior to scintillation counting, skewing results. Further use of iGlucoSnFR, especially in more physiologically significant *in vivo* preparations, may be able to resolve these discrepancies, but at a minimum, the efficacy and utility of iGlucoSnFR in cultured preparations is demonstrated by the current data.

### Characterization in larval fly central nervous system (CNS) explant

To demonstrate the utility of the sensor in intact systems, we created a transgenic *lexAOp-iGlucoSnFR-mRuby2 Drosophila* line. After balancing, this fly line was crossed with the *57C10-lexA* driver line (Pfeiffer et al., 2012) to establish pan-neuronal expression. Whole CNSs (including brain lobes and the ventral nerve cord [VNC]) were excised from third instar larvae and mounted either directly on the coverslip-bottomed dish or in a thin layer of 1% agarose to mechanically stabilize the preparation. Buffers with or without 20 mM glucose were oscillated with a periodicity of 10 min (Figure 3A). Confocal volumetric time-lapse imaging ( $8 \times 5$ - $\mu$ m planes,  $1,024 \times 512$  pixels,  $\sim 9$  s/vol) of these brains (Data S2) showed increases in glucose concentration throughout the whole explant, with much greater changes in the VNC than in the brain lobes (Figure 3B). Glucose concentrations (Figure 3C) rose most quickly in the rostral VNC neuropil (and some large nerves—although since they have been severed by the dissection, this is likely non-physiological). A wave of glucose sensor response moved caudally within the VNC neuropil, and eventually outward to the surrounding neuronal cell bodies. The rostro-caudal peak-to-peak delay in the neuropil was about 30 s, or three volumetric frames, and was observed in all optical sections. Influx into the brain lobes was delayed relative to the rostral VNC and appeared similarly to proceed from the inside outward. These unexpected results were reproducible across individual larvae (Figure 3D;  $n = 5$ ) and were independent of perfusion direction or agarose embedding.

### *In vivo* characterization in zebrafish larvae

Transparent larval zebrafish are excellent preparations for *in vivo* imaging; furthermore, the ease with which they take up drugs from their water makes simultaneous imaging and pharmacology straightforward. A stable zebrafish transgenic line, *Tg(actb2: iGlucoSnFR)*, was generated to express iGlucoSnFR broadly throughout the animal using the  $\beta$ -*actin* promoter. Larval (5–6 days post-fertilization [dpf]) fish were embedded in agar (no anesthesia or paralysis) and imaged volumetrically on a confocal microscope (15 sections at 15- $\mu$ m thickness,  $512 \times 256$  pixels,  $\sim 10$  s/vol). During initial characterization, it became apparent

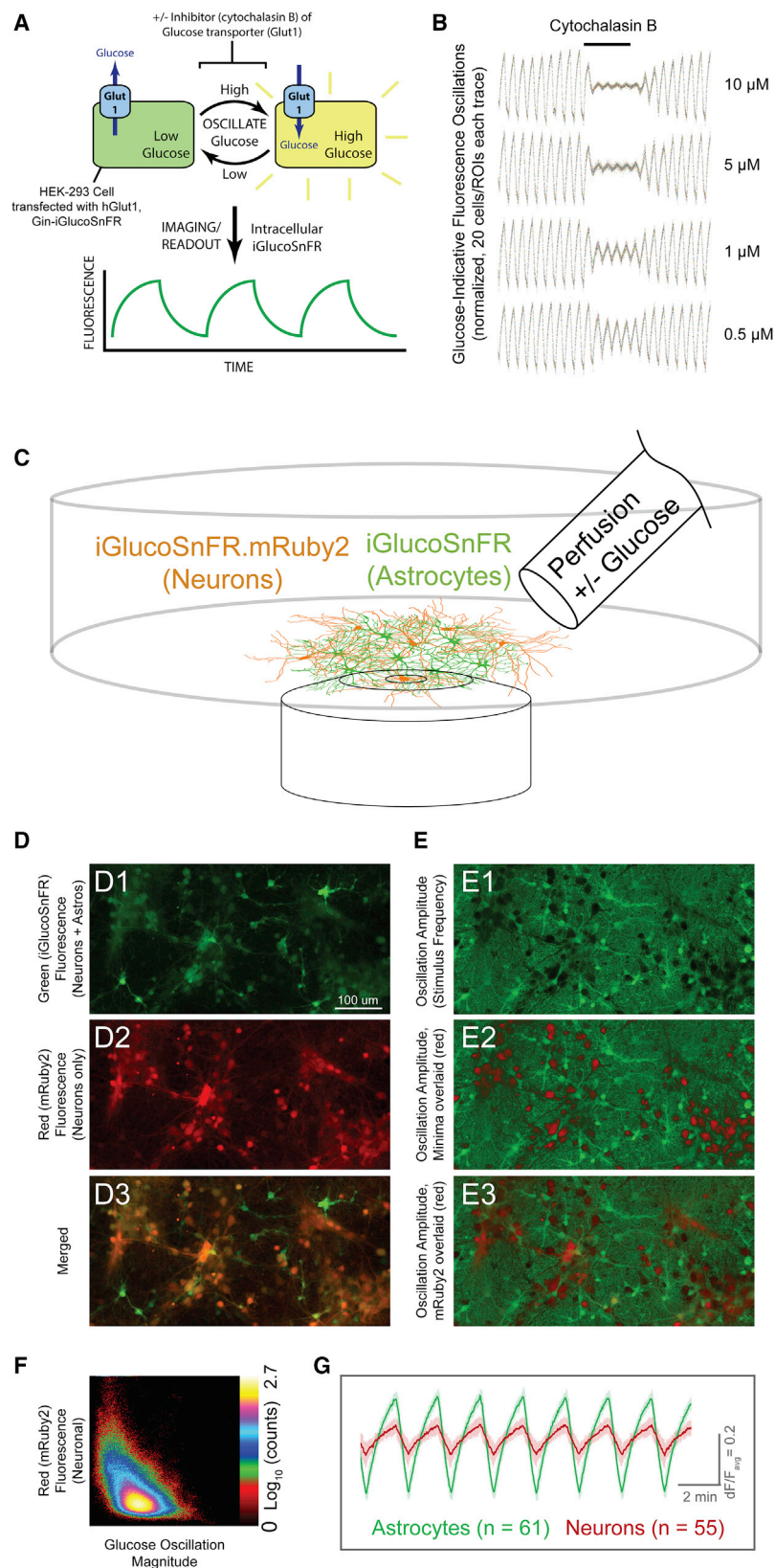


**Figure 2. Sensor applications in cell culture**

(A) Schematic of transporter assay. Cultured cells (HEK293) were co-transfected with plasmids for expression of iGlucoSnFR and the human glucose uniporter hGlut1. Buffers were oscillated with and without glucose, eliciting oscillating fluorescence responses, which were subsequently diminished by overlaying constant concentrations of the glucose transporter inhibitor cytochalasin B at various concentrations.

(B) Oscillating fluorescence responses and inhibition. Twenty regions of interest (ROIs) corresponding to cells were identified by fast Fourier transform (FFT) magnitude in initial segments without inhibitor and were filtered over the whole experiment by subtraction of a moving-window average of length corresponding to the stimulus period. Each trace was then normalized by root-mean-square deviation (RMSD) during the pre-treatment phase and plotted as individual data points. In the middle segment (indicated at top), cytochalasin B was added at the concentrations indicated at the right of each trace. After removing cytochalasin B, oscillation magnitudes returned to initial values. Imaging parameters were: two channels: excitation (Ex) 488 nm, emission (Em) 505–550; Ex 561, Em 565–650; objective EC Plan-Neofluar 10×/0.3 numerical aperture (NA) M27, imaging rate ~1 Hz; 512 × 512 pixels; stimulus period 60 s.

(C) Schematic of neuronal culture assay. Acute astrocyte-neuron co-cultures from rat hippocampus were infected with AAVs driving iGlucoSnFR-mRuby2 expression in neurons (*hSynapsin-1* promoter) and green-only iGlucoSnFR in astrocytes (*gfaABC,D* promoter). ACSF + 20 mM glucose or sorbitol was continuously perfused, and fluorescence changes were measured.

(D and E) Fluorescence imaging of co-cultures. (D1–D3) Fluorescence images for each channel are shown as indicated. (E1–E3) Images of pixelwise temporal FFT magnitudes at stimulus frequency, indicative of glucose concentration changes. E1 shows amplitudes in green. E2 shows the same image but with FFT minima overlaid in red, for comparison with the mRuby2 signals overlaid in E3 (also see alone in D2). Two channels: Ex 488 nm, Em 505–550; Ex 561, Em 565–650; objective Plan-Apochromat 20×/0.8 NA M27, imaging rate ~1 Hz; 1,024 × 512 pixels; stimulus period 120 s.

(F) Correlation plot between FFT magnitude (x axis) and mRuby2 signal (y axis). Note clear (albeit weak) anti-correlation between the two (correlation coefficient [CC] of ~-0.5): high intensity in the red channel corresponds to weak magnitudes and vice versa.

(G) Averaged fluorescence responses ( $\Delta F/F_{avg}$ ) to oscillating stimulus from astrocytes (identified by high-thresholded green/red fluorescence ratio) and neurons (identified by high red fluorescence signals).  $\Delta F/F_{avg}$  was calculated by subtraction of a moving window average with size corresponding to the period of the stimulus oscillations followed by division by the same moving average. Note the larger magnitude of glucose response in astrocytes. Error bars represent SD in fluorescence responses within each group. Nearly identical results with reversed tags are shown in Figure S2.

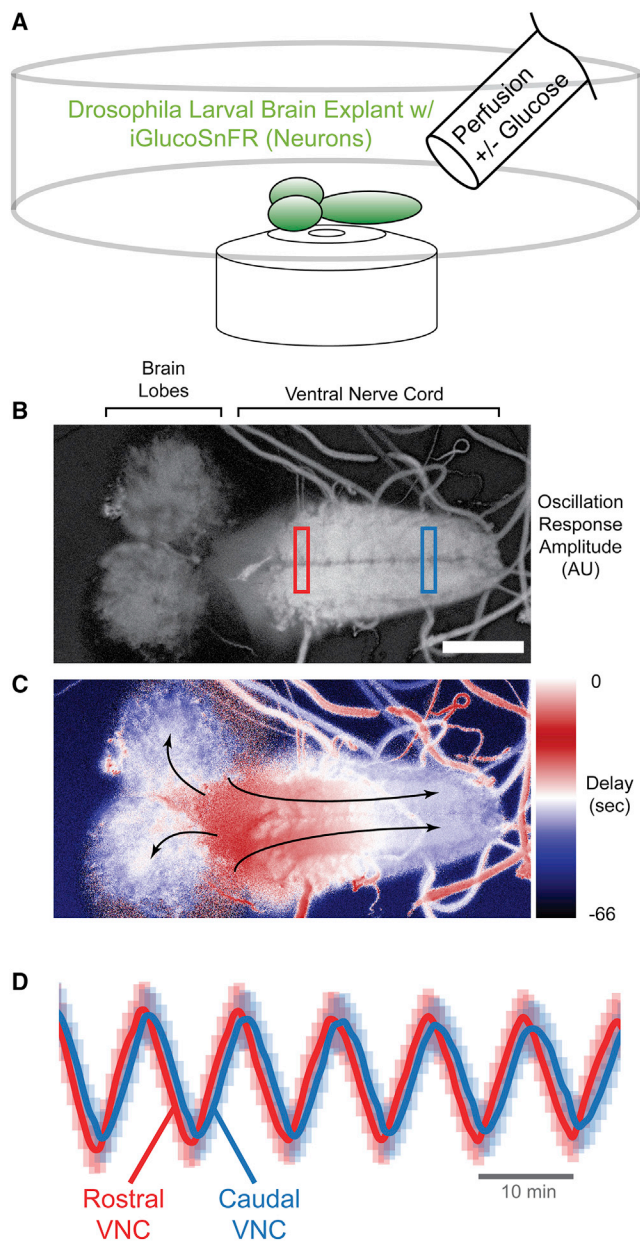


**Figure 3. Sensor application in intact larval fruit fly CNS explant**

(A) Schematic of assay. Third-instar larval fly CNS expressing iGlucoSnFR-mRuby2 in all neurons (*57C10* driver), embedded in a thin layer of 1% agar, were subjected to continuous perfusion with and without glucose under continuous volumetric confocal imaging. Eight planes at 4.8- $\mu$ m steps; two channels: Ex 488 nm, Em 505–550; Ex 561, Em 565–650; objective Plan-Apochromat 20 $\times$ /0.8 NA M27, imaging rate  $\sim$ 9 s per volume; 1,024  $\times$  512 pixels; stimulus period 10 min. Scale bar, 100  $\mu$ m.

(B) FFT amplitudes of response. Time-lapse intensity-normalized average projections in z were subjected to pixelwise temporal FFT. Magnitudes at stimulus frequency were extracted and are represented in grayscale.

(C) FFT phases/delays of response. Similar to (B), but here stimulus frequency phases were extracted, revealing a temporal gradient in glucose response along the axis of the VNC neuropil and to a lesser extent in the brain lobes (arrows indicate direction of response).

that not only did spontaneous muscle twitches of the agar-mounted fish affect intracellular glucose in muscle, but also that these responses were different in fed versus unfed fish. Thus, a stable *Tg* (*acta1a*: jRGECO1a) line was generated as well, expressing the red genetically encoded calcium indicator jRGECO1a (*Dana et al., 2016*) in skeletal muscle with the  $\alpha$ -*actinin* promoter. Crossing these two lines yielded *Tg* (*actb2*: iGlucoSnFR; *acta1a*: jRGECO1a), allowing simultaneous measurement of glucose uptake (green) into all cells and action potential firing and accompanying  $\text{Ca}^{2+}$  uptake (red) into muscles.

Confocal imaging of the double transgenic line revealed intriguing relationships between muscle twitching and glucose uptake in different body regions. In unfed fish, calcium spikes in muscle were always followed by a graded rise in intracellular glucose, which then gradually returned to baseline (Figure 4A, top; Data S3A). The largest glucose uptake events seemed to follow the largest muscle spikes (Figure 4A, top). (We did not quantify this effect due to the relatively slow temporal resolution of the volumetric confocal imaging, which hampered measurement of the exact timing and magnitude of jRGECO1a spikes.) In fed fish, however, glucose levels appeared steady regardless of muscle twitching (small, short-lived responses were seen, but might be movement artifacts; Figure 4A, bottom). This is likely due to higher extracellular and intracellular resting glucose levels enabling cells to recover more quickly in the fed state.

The hormone insulin increases glucose uptake in skeletal muscles. Upon injection of human insulin directly into the posterior caudal vein of *Tg* (*actb2*: iGlucoSnFR) fish, large increases in intramuscular glucose were observed (Figures 4B and 4C; Data S3B) with a rise time to half-maximum of about 4–6 min (Figure 4C), consistent with results in cultured muscle cells (Stand-aert et al., 1984). Saline-only injections did not elicit any response (Figure 4C: early part of traces). The hormone epinephrine also has a potent effect on glucose metabolism in muscles: it stimulates glycogenolysis and inhibits glycogen production, leading to high intracellular concentrations of glucose-6-phosphate to feed into augmented glycolysis. At the same time, epinephrine increases systemic glucose rapidly through mobilization of glycogen stores in the liver into glucose followed by efflux into the circulatory system. Addition of epinephrine to the bath of *Tg* (*actb2*: iGlucoSnFR; *acta1a*: jRGECO1a) fish led to dramatic increases in intramuscular glucose levels within about 2 min (Figures 4D and 4E; Data S3C–E), presumably the time necessary to diffuse through the agar and into the fish. About 5 min after the initial rise in intramuscular glucose, the fish began to twitch more frequently, and jRGECO1a indicated more muscle spiking (Figure 4E), consistent with “physiological tremor” known to be induced by epinephrine (Bowman, 1981). It is noteworthy that glucose increases began several minutes before calcium spikes appeared, allowing for the possibility that glucose itself might play a role in spawning the observed muscular fasciculations.

Since the liver is an organ central to glucose physiology, and since the aforementioned transgenic fish did not show detectable sensor expression in the liver, we generated transgenic

(D)  $\Delta F/F_{\text{avg}}$  traces from VNC. Normalized fluorescence traces from rectangular regions of interest at rostral or caudal ends of VNC as indicated. Note phase shift. Error bars represent SD of pixels within each ROI.

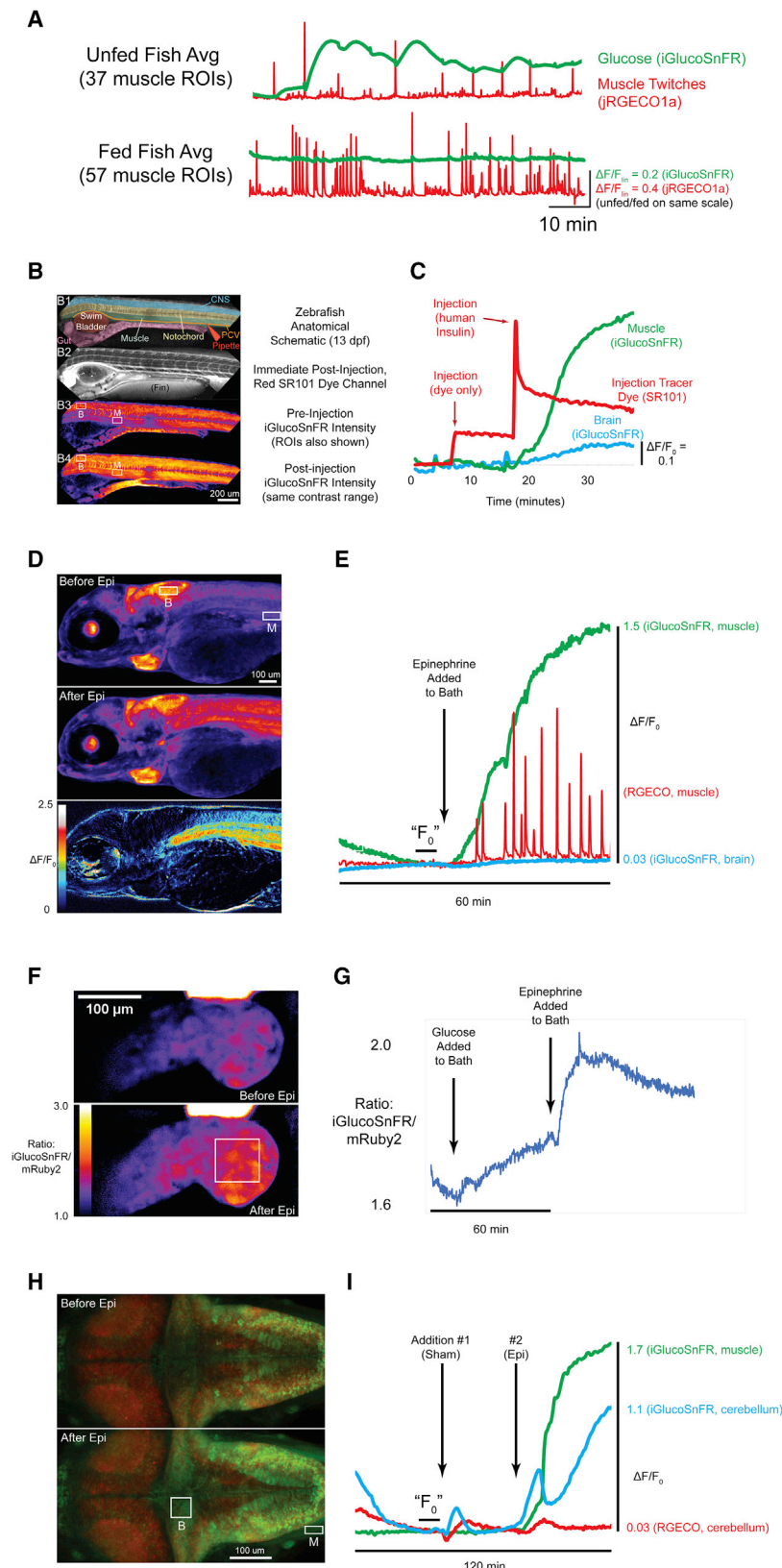


**Figure 4. Sensor application in zebrafish muscle and brain *in vivo***

(A) Glucose responses to spontaneous muscle twitches. We generated a zebrafish line that expresses iGlucoSnFR broadly ( $\beta$ -actin promoter) and the red calcium indicator jRGECO1a in muscle ( $\alpha$ -actinin promoter). Non-anesthetized, non-paralyzed fish were imaged 5–6 days post-fertilization (dpf) for spontaneous responses to muscle twitches. Representative averaged traces from volumetric time-lapse confocal imaging of fed and never-fed fish are presented as indicated.  $F_{in}$ , fluorescence response divided by a linear baseline.

(B) Imaging of insulin responses. 13 dpf zebrafish broadly expressing iGlucoSnFR ( $\beta$ -actin promoter) are shown. (B1) Schematic illustrating anatomy. Note injection pipette poised for injection into the posterior cardinal vein (PCV). (B2) Red fluorescence channel immediately post-injection with insulin and sulforhodamine-101 (SR101) as a marker dye. The entire vasculature became transiently fluorescent red after injection, demonstrating efficacy of systemic injection. (B3 and B4) iGlucoSnFR fluorescence before and after insulin injection. ROIs on brain (“B”) and muscle (“M”) as indicated are plotted in (C). Two channels: Ex 488 nm, Em 505–550; Ex 561, Em 565–650; objective EC Plan-Neofluar 10 $\times$ /0.3 NA M27, imaging rate  $\sim$ 1 s per image; 512  $\times$  512 pixels.

(C) Insulin-induced fluorescence changes. Red trace indicates injection of dye or dye plus insulin. Green trace indicates iGlucoSnFR fluorescence measured from muscle (ROI “M” in panel B). Blue trace indicates iGlucoSnFR fluorescence measured from brain (ROI “B” in panel B). Small, artifactual changes in fluorescence appear with introduction of the pipette (dye-only injection). Sustained fluorescence increases arise after insulin injection.

(D) Imaging organism-scale responses of iGlucoSnFR to epinephrine addition. 5 dpf fish expressing both iGlucoSnFR (all cells,  $\beta$ -actin promoter) and jRGECO1a (muscle cells,  $\alpha$ -actinin promoter). Top two images (before and after epinephrine, sagittal section) show false-color raw intensities from a volumetric time-lapse iGlucoSnFR movie average-projected in z. ROIs on muscle (“M”) and brain (“B”) are plotted in (E). Bottom image shows  $\Delta F/F_0$  after addition of epinephrine, with muscle showing the greatest changes. 5 dpf; 15 planes at 15- $\mu$ m steps; two channels: Ex 488 nm, Em 505–550; Ex 561, Em 565–650; objective EC Plan-Neofluar 10 $\times$ /0.3 NA M27, imaging rate  $\sim$ 10 s per volume; 512  $\times$  256 pixels.

(E) Epinephrine-induced fluorescence changes. Blue trace indicates iGlucoSnFR fluorescence measured from hindbrain (ROI “B” in panel D). Green trace indicates iGlucoSnFR fluorescence measured from muscle (ROI “M” in panel D). Red trace indicates jRGECO1a fluorescence measured from the same muscle ROI.  $F_0$  was defined as the averaged intensity value just before addition of epinephrine to the bath, as indicated. Note the delayed increase of neuronal activity subsequent to glucose increases.

(F) Liver iGlucoSnFR responses to glucose and epinephrine. Ratio image (iGlucoSnFR/mRuby2) is shown of average of two confocal places (20  $\mu$ m total) over eight time points (80 s) of a 7 dpf fish expressing mRuby-tagged iGlucoSnFR in liver (*fabp10a* promoter) before and after epinephrine addition. Plotted area in (G) is indicated by white box. 20 planes at 10- $\mu$ m steps; two channels: Ex 488 nm, Em 505–550; Ex 561, Em 565–650; objective (legend continued on next page)

fish with a reported liver-specific promoter (Denovan-Wright et al., 2000), fatty acid-binding protein 10a (*FABP10a*), driving expression of mRuby2-tagged intracellular sensor. Since the liver is quite mobile and elastic compared to muscle, the mRuby2-tagged sensor was found to be more reliable for detection of glucose fluctuations. We treated fish first with glucose (40 mM) and subsequently with epinephrine (1 mM). Addition of glucose evoked only a moderate but detectable increase in fluorescence, whereas epinephrine addition markedly increased signal (Figures 4F and 4G; Data S3F). These results are consistent with the role of the liver in uptake/storage of glucose as glycogen (initial glucose-only stimulus) and the liver's response to epinephrine in mobilization of glucose (epinephrine stimulus).

In a fourth set of experiments, epinephrine effects on brain function were monitored by imaging *Tg* (*actb2*: iGlucoSnFR; *HuC/elav3*: jRGECO1a) fish. Although changes in brain glucose were difficult to discern in the lower magnification experiments above, it seemed likely that a more detailed investigation at higher magnification might reveal changes. Indeed, upon a sham addition of fish water into the bath, several brain regions (notably cerebellum and hindbrain; Figure 4H) showed immediate responses in both imaging channels, indicating transient increases in neuronal firing and glucose uptake (Figures 4H and 4I; Data S3G and H). Muscle tissue in the same field of view showed no response to sham addition. Subsequent addition of epinephrine to the bath led to immediate jRGECO1a and iGlucoSnFR responses in the brain, similar to the sham addition. iGlucoSnFR fluorescence, however, showed a larger and continued increase, as did muscle-expressed iGlucoSnFR (Figure 4I). Sample deformation in the brain upon epinephrine addition, albeit moderate, precluded precise mapping of intensity changes, but visual inspection and cross-checking intensity changes of neighboring regions in x, y, and z dimensions indicated that the changes were appreciable and not artifactual. Thus, although some brain effects arise from fluid flow, the largest increases in brain and all muscle effects are specific to epinephrine addition.

## DISCUSSION

We have presented a series of genetically encoded, single-wavelength sensors for glucose, with affinities ranging from 1  $\mu$ M to 10 mM. They can be easily targeted to specific populations of cells and to sub-cellular compartments to visualize changes in glucose concentration in preparations from cultured cells to intact living animals. They are amenable to long-term expression and imaging. The microbial nature of the binding pro-

tein likely renders them otherwise biologically inert in plants and animals. Due to the high glucose concentrations in most situations of interest, buffering by the sensor is negligible. Their single-wavelength nature makes them easy to image and compatible with simultaneous imaging of other physiological phenomena in a separate color channel. Fusion of the red fluorescent protein mRuby2 allows ratiometric imaging for samples with motion artifacts, or simultaneous imaging of two cell types, as shown here with neurons and astrocytes. iGlucoSnFR could be targeted to sub-cellular compartments, the outer plasma membrane, and so forth with the appropriate leader and/or fusion peptides.

Single-wavelength sensors such as iGlucoSnFR and FRET indicators such as FLIPglu have distinct advantages and disadvantages (Leavesley and Rich, 2016; Piston and Kremers, 2007). FRET sensors incorporate two fluorescent proteins, which increases indicator size and inherently limits signal changes, as most of the useful FRET distance is taken up by the probes themselves. FRET ratioing (sensitized emission) can partially compensate for sample motion and differences in sensor concentration, but it requires image correction for donor-acceptor crosstalk, slows down imaging rates, convolves two error sources, and requires complicated equipment. The use of two fluorescent proteins uses more spectral bandwidth and introduces differential photostability, pH sensitivity (Betolngar et al., 2015), chromophore maturation, and light penetration, which alter the FRET ratio independent of ligand. Single-wavelength sensors have larger signal changes, high enough to provide robust *in vivo* imaging in freely moving animals with no second color channel or motion correction (Skocek et al., 2018; Vaadia et al., 2019). The very large signal change of single-wavelength indicators also gives them greater photostability, as the sensor can only bleach in the bright state, as opposed to FRET sensors, where donor and acceptor are always bright and bleach-prone (Tian et al., 2009). On the other hand, sensors based on circularly permuted fluorescent proteins typically have higher acid dissociation constant ( $pK_a$ ) values than do the unpermuted parents and are thus more pH-sensitive. In related work, we have engineered a fluorescence lifetime imaging (FLIM)-compatible version of the sensor, iGlucoSnFR-TS (Diaz-García et al., 2019), based on the fluorescent protein T-Sapphire, which facilitates more quantitative [glucose] determination in various preparations, including in living mice.

The use of iGlucoSnFR with the oscillating stimulus transporter assay (OSTA) (Keller and Looger, 2016) allows precise and rapid measurement of glucose transporter properties. In this study, we showed both Glut1-mediated glucose transport and inhibition by CCB, which recapitulated previous

Plan-Apochromat 20 $\times$ /0.8 NA M27, imaging rate  $\sim$ 10 s per volume; 1,024  $\times$  512 pixels.

(G) Glucose and epinephrine-induced fluorescence ratio changes in liver. Glucose and epinephrine were added to bath at indicated times. ROIs adjacent in x, y, and z showed similar responses.

(H) Imaging brain-scale epinephrine responses. Single coronal section confocal plane (after stack registration) is shown of a 5 dpf fish expressing both iGlucoSnFR (all cells,  $\beta$ -actin promoter) and jRGECO1a (neurons, *elav3* promoter) before and after epinephrine addition. ROIs on muscle ("M") and cerebellum ("B") are plotted in (I). 5 dpf; 40 planes at 3.3- $\mu$ m steps; two channels: Ex 488 nm, Em 505–550; Ex 561, Em 565–650; objective Plan-Apochromat 20 $\times$ /0.8 NA M27, imaging rate  $\sim$ 25 s per volume; 512  $\times$  256 pixels.

(I) Epinephrine-induced fluorescence changes in the brain. Green trace indicates iGlucoSnFR fluorescence measured from muscle (ROI "M" in panel H). Blue trace indicates iGlucoSnFR fluorescence measured from cerebellum (ROI "B" in panel H). Red trace indicates jRGECO1a fluorescence from same cerebellum ROI.  $F_0$  was derived from the averaged intensity values just before addition of epinephrine to the bath.

determinations of  $IC_{50}$ . Typically, glucose transporters have been studied with radiolabeled substrates or fluorescent dyes. Radioisotope measurements are hampered by poor spatial and temporal resolution, and thus preclude longitudinal monitoring of transport rates. Fluorescent glucose analogs have different rates of transport between transporters relative to unmodified glucose and can produce misleading results. Robust genetically encoded sensors make these measurements straightforward. The ability of the sensors to produce large fluorescent responses to unmodified glucose ensures accuracy of the results. The amenability of the sensors to prolonged longitudinal imaging also facilitates the tracking of glucose transport across a range of physiological perturbations, such as cytosolic signaling pathways, extracellular factors, pharmacological agents, or endocytosis/exocytosis of transporter populations.

iGlucoSnFR revealed greater glucose uptake in astrocytes than in neurons in co-culture. This phenomenon has been previously described using glucose analogs (Hara et al., 1989; Lundgaard et al., 2015), but those results were ambiguous due to the glucose analog having different transport rates among transporter types (i.e., between Glut3, the primary neuronal glucose transporter, and Glut1, the primary astrocyte glucose transporter). The differences in glucose transport rates observed in culture may have ramifications for the ongoing discussion concerning the nature of neuronal metabolism, and particularly the astrocyte-neuron lactate shuttle hypothesis (ANLSH) (Pellerin and Magistretti, 1994).

The glucose disaccharide trehalose ( $\alpha$ -1-D-glucopyranosyl- $\alpha$ -1-D-glucopyranoside) is the most prominent sugar in *Drosophila* hemolymph (Wyatt and Kalf, 1957), but lower levels of glucose are also present. Nevertheless, metabolic energy is generated through glucose, which is readily produced through trehalose cleavage. In *Drosophila* CNS explants, our experiments using iGlucoSnFR showed that, contrary to expectations for a simple diffusion model of glucose flux, interior parts of the CNS saw increases in intracellular glucose concentration before bath-exposed, external regions. This paradoxical pattern in CNS glucose uptake suggests that the glial hemolymph-brain barrier (HBB) is intact in the preparation. It remains doubtful, however, that the HBB should be impermeable to a metabolic constituent as significant as glucose. In fact, it has been shown that in larval brains, HBB cells and other glial cells do import glucose (Volkenhoff et al., 2018). It is possible that the glia constituting the HBB, which do not express iGlucoSnFR in the current preparation, may be taking up glucose and converting it to lactate or alanine for supplying neurons with metabolic energy, consistent with the ANLSH (Pellerin and Magistretti, 1994), as had been suggested previously (Volkenhoff et al., 2015). While this is occurring, an alternative “inside-out” pathway of direct glucose trafficking, observed herein, may be providing neurons with glucose per se. This would suggest that neurons use both lactate and glucose as energy sources—consistent with an emerging consensus that both neuronal energy sources are used to varying degrees—but through different transport pathways. It remains to be seen whether the observed rostro-caudal glucose pathway is present *in vivo*, what its mechanism and function might be, and

exactly where and how glucose enters the CNS. Since the origin of the apparent glucose waves is near the esophageal foramen, which is surrounded by glucose-relevant *Drosophila* insulin-like peptide (DILP) neurons (Nässel et al., 2013), it may be speculated that the esophageal foramen provides a direct port of entry for glucose per se into the CNS. Nevertheless, identification of spatiotemporal glucose trafficking patterns such as this is currently only possible through the use of iGlucoSnFR and other similar sensors; it will be interesting to see what other spatiotemporal patterns will be found through their use.

In zebrafish larvae, iGlucoSnFR reported insulin- and epinephrine-induced increases in muscle, liver, and brain glucose. These changes paralleled neuronal and muscle activity as reported by multiplexed imaging with the calcium sensor jRGECO1a. We expect higher resolution correlations between calcium and glucose signals to be achieved with faster and more spatially resolved volumetric imaging (Lemon et al., 2015). Zebrafish expressing iGlucoSnFR could provide an experimentally tractable method for investigating the details of exercise-mediated glucose uptake in both muscle and liver, which is obviously of high medical relevance to both obesity and diabetes. Furthermore, any organ of interest, such as heart, can also be targeted using specific promoters (e.g., *cryaa* in the case of heart).

Many important questions about glucose regulation remain incompletely answered. What are the precise molecular mechanisms by which circulatory glucose levels are correctly sensed, leading to insulin or glucagon secretion from the pancreas? What is the contribution of the various pancreatic cell types (Gylfe, 2016; Rutter et al., 2015)? What initiates impaired glucose tolerance and how does this result in insulin resistance? What is the role of intestinal gluconeogenesis and how is gut-brain-pancreas glucose sensing coordinated (Soty et al., 2017)? What is the interplay between glucose dyshomeostasis and autoimmune disease (Dessein and Joffe, 2006)? These questions need tools for measuring glucose with high spatial and temporal resolution, and iGlucoSnFR will undoubtedly be useful for their study.

## STAR★METHODS

Detailed methods are provided in the online version of this paper and include the following:

- KEY RESOURCES TABLE
- RESOURCE AVAILABILITY
  - Lead contact
  - Materials availability
  - Data and code availability
- EXPERIMENTAL MODEL AND SUBJECT DETAILS
  - HEK293 cells
  - Flies
  - Zebrafish
  - Rats for generation of cultured neurons and astrocytes
- METHOD DETAILS
  - Cloning and mutagenesis
  - Protein purification
  - Stopped-flow fluorescence
  - Mutant screening

- Cultured HEK293 cells
- Cultured neurons/astrocytes
- Perfusion system
- AAVs
- Flies
- Zebrafish
- Imaging and image processing: HEK cells
- Imaging and image processing: neuron/astrocyte co-cultures
- Imaging and image processing: *Drosophila* CNS
- Imaging and image processing: Zebrafish larvae
- **QUANTIFICATION AND STATISTICAL ANALYSIS**

### SUPPLEMENTAL INFORMATION

Supplemental information can be found online at <https://doi.org/10.1016/j.celrep.2021.109284>.

### ACKNOWLEDGMENTS

We would like to thank Jay Unruh for ImageJ plugins; Gary Yellen, Jim Truman, Tim Ryan, and Phil Borden for helpful discussions; Deepika Walpita and Kathy Schaefer for cell culture; the Janelia Fly Facility for fly maintenance; and Jared Rouchard & the Janelia Aquarium Facility for zebrafish maintenance. We thank Dr. Michael Pack (University of Pennsylvania) for the kind gift of p5E-*fabp10a*. We thank Gaby Paez for help making the graphical abstract. This work was funded by the Howard Hughes Medical Institute.

### AUTHOR CONTRIBUTIONS

J.P.K., J.S.M., S.K., R.T.L., and L.L.L. conceived, designed, and constructed the sensor and variations thereof. J.P.K., J.S.M., and S.K. characterized the sensor in purified protein. J.P.K., J.S.M., H.L., W.C.L., J.S., M.K., P.J.K., and L.L.L. contributed to the design of cellular and animal experiments. J.P.K., J.S., H.L., and W.C.L. generated experimental animals, prepared, and/or conducted physiological experiments. J.P.K., J.S.M., W.C.L., M.K., and L.L.L. analyzed the data. J.P.K., J.S.M., and L.L.L. wrote the manuscript, with input from the other authors.

### DECLARATION OF INTERESTS

L.L.L., J.S.M., and R.T.L. are holders of US Patent US9939437B2, which covers iGlucoSnFR. The remaining authors declare no competing interests.

Received: April 8, 2019

Revised: March 6, 2020

Accepted: June 1, 2021

Published: June 22, 2021

### REFERENCES

Alicea, I., Marvin, J.S., Miklos, A.E., Ellington, A.D., Looger, L.L., and Schreiter, E.R. (2011). Structure of the *Escherichia coli* phosphonate binding protein PhnD and rationally optimized phosphonate biosensors. *J. Mol. Biol.* *414*, 356–369.

Ashrafi, G., and Ryan, T.A. (2017). Glucose metabolism in nerve terminals. *Curr. Opin. Neurobiol.* *45*, 156–161.

Ashrafi, G., Wu, Z., Farrell, R.J., and Ryan, T.A. (2017). GLUT4 mobilization supports energetic demands of active synapses. *Neuron* *93*, 606–615.e3.

Betoltinger, D.-B., Erard, M., Pasquier, H., Bousmah, Y., Diop-Sy, A., Guiot, E., Vincent, P., and Mérola, F. (2015). pH sensitivity of FRET reporters based on cyan and yellow fluorescent proteins. *Anal. Bioanal. Chem.* *407*, 4183–4193.

Bittner, C.X., Lozaiza, A., Ruminot, I., Larenas, V., Sotelo-Hitschfeld, T., Gutiérrez, R., Córdova, A., Valdebenito, R., Frommer, W.B., and Barros, L.F. (2010).

High resolution measurement of the glycolytic rate. *Front. Neuroenergetics* *2*, 26.

Borden, P.M., Zhang, P., Shivange, A.V., Marvin, J.S., Cichon, J., Dan, C., Podgorski, K., Figueiredo, A., Novak, O., Tanimoto, M., et al. (2020). A fast genetically encoded fluorescent sensor for faithful in vivo acetylcholine detection in mice, fish, worms and flies. *Biorxiv* *16*, 2020.02.07.939504.

Bowman, W.C. (1981). Effects of adrenergic activators and inhibitors on the skeletal muscles. In *Adrenergic Activators and Inhibitors, Part II*, L. Szekeres, ed. (Springer), pp. 47–128.

Braun, S., Bitton-Worms, K., and LeRoith, D. (2011). The link between the metabolic syndrome and cancer. *Int. J. Biol. Sci.* *7*, 1003–1015.

Chen, L.-Q., Hou, B.-H., Lalonde, S., Takanaga, H., Hartung, M.L., Qu, X.-Q., Guo, W.-J., Kim, J.-G., Underwood, W., Chaudhuri, B., et al. (2010). Sugar transporters for intercellular exchange and nutrition of pathogens. *Nature* *468*, 527–532.

Cuneo, M.J., Changela, A., Warren, J.J., Beese, L.S., and Hellinga, H.W. (2006). The crystal structure of a thermophilic glucose binding protein reveals adaptations that interconvert mono and di-saccharide binding sites. *J. Mol. Biol.* *362*, 259–270.

Dana, H., Mohar, B., Sun, Y., Narayan, S., Gordus, A., Hasseman, J.P., Tsegaye, G., Holt, G.T., Hu, A., Walpita, D., et al. (2016). Sensitive red protein calcium indicators for imaging neural activity. *eLife* *5*, 413.

Denovan-Wright, E.M., Pierce, M., Sharma, M.K., and Wright, J.M. (2000). cDNA sequence and tissue-specific expression of a basic liver-type fatty acid binding protein in adult zebrafish (*Danio rerio*). *Biochem. Biophys. Acta* *1492*, 227–232.

Dessein, P.H., and Joffe, B.I. (2006). Insulin resistance and impaired beta cell function in rheumatoid arthritis. *Arthritis Rheum.* *54*, 2765–2775.

Deuschle, K., Okumoto, S., Fehr, M., Looger, L.L., Kozhukh, L., and Frommer, W.B. (2005). Construction and optimization of a family of genetically encoded metabolite sensors by semirational protein engineering. *Protein Sci.* *14*, 2304–2314.

Díaz-García, C.M., Lahmann, C., Martínez-François, J.R., Li, B., Koveal, D., Nathwani, N., Rahman, M., Keller, J.P., Marvin, J.S., Looger, L.L., and Yellen, G. (2019). Quantitative in vivo imaging of neuronal glucose concentrations with a genetically encoded fluorescence lifetime sensor. *J. Neurosci. Res.* *97*, 946–960.

Fehr, M., Lalonde, S., Lager, I., Wolff, M.W., and Frommer, W.B. (2003). In vivo imaging of the dynamics of glucose uptake in the cytosol of COS-7 cells by fluorescent nanosensors. *J. Biol. Chem.* *278*, 19127–19133.

Ge, X., Tolosa, L., and Rao, G. (2004). Dual-labeled glucose binding protein for ratiometric measurements of glucose. *Anal. Chem.* *76*, 1403–1410.

Guilbault, G.G., and Lubrano, G.J. (1973). An enzyme electrode for the amperometric determination of glucose. *Anal. Chim. Acta* *64*, 439–455.

Gylfe, E. (2016). Glucose control of glucagon secretion — “There’s a brand-new gimmick every year”. *Ups. J. Med. Sci.* *121*, 120–132.

Hara, M., Matsuda, Y., Hirai, K., Okumura, N., and Nakagawa, H. (1989). Characteristics of glucose transport in neuronal cells and astrocytes from rat brain in primary culture. *J. Neurochem.* *52*, 902–908.

Higashijima, S., Okamoto, H., Ueno, N., Hotta, Y., and Eguchi, G. (1997). High-frequency generation of transgenic zebrafish which reliably express GFP in whole muscles or the whole body by using promoters of zebrafish origin. *Dev. Biol.* *192*, 289–299.

Hu, H., Gu, Y., Xu, L., Zou, Y., Wang, A., Tao, R., Chen, X., Zhao, Y., and Yang, Y. (2017). A genetically encoded toolkit for tracking live-cell histidine dynamics in space and time. *Sci. Rep.* *7*, 43479.

Hu, H., Wei, Y., Wang, D., Su, N., Chen, X., Zhao, Y., Liu, G., and Yang, Y. (2018). Glucose monitoring in living cells with single fluorescent protein-based sensors. *RSC Advances* *8*, 2485–2489.

Jahreis, K., Pimentel-Schmitt, E.F., Brückner, R., and Titgemeyer, F. (2008). Ins and outs of glucose transport systems in eubacteria. *FEMS Microbiol. Rev.* *32*, 891–907.

- Kapoor, K., Finer-Moore, J.S., Pedersen, B.P., Caboni, L., Waight, A., Hillig, R.C., Bringmann, P., Heisler, I., Müller, T., Siebeneicher, H., and Stroud, R.M. (2016). Mechanism of inhibition of human glucose transporter GLUT1 is conserved between cytochalasin B and phenylalanine amides. *Proc. Natl. Acad. Sci. USA* *113*, 4711–4716.
- Kaur, J. (2014). Retracted. *Cardiol. Res. Pract.* *2019*, 4301528.
- Kawakami, K., Takeda, H., Kawakami, N., Kobayashi, M., Matsuda, N., and Mishina, M. (2004). A transposon-mediated gene trap approach identifies developmentally regulated genes in zebrafish. *Dev. Cell* *7*, 133–144.
- Keller, J.P., and Looger, L.L. (2016). The oscillating stimulus transporter assay, OSTA: Quantitative functional imaging of transporter protein activity in time and frequency domains. *Mol. Cell* *64*, 199–212.
- Kunkel, T.A. (1998). Oligonucleotide-directed mutagenesis without phenotypic selection. *Curr. Protoc. Neurosci.*, Chapter 4:Unit 4.10.
- Lam, A.J., St-Pierre, F., Gong, Y., Marshall, J.D., Cranfill, P.J., Baird, M.A., McKeown, M.R., Wiedenmann, J., Davidson, M.W., Schnitzer, M.J., et al. (2012). Improving FRET dynamic range with bright green and red fluorescent proteins. *Nat. Methods* *9*, 1005–1012.
- Leavesley, S.J., and Rich, T.C. (2016). Overcoming limitations of FRET measurements. *Cytometry A* *89*, 325–327.
- Lemon, W.C., Pulver, S.R., Höckendorf, B., McDole, K., Branson, K., Freeman, J., and Keller, P.J. (2015). Whole-central nervous system functional imaging in larval *Drosophila*. *Nat. Commun.* *6*, 7924.
- Low Wang, C.C., Hess, C.N., Hiatt, W.R., and Goldfine, A.B. (2016). Clinical update: cardiovascular disease in diabetes mellitus: Atherosclerotic cardiovascular disease and heart failure in type 2 diabetes mellitus—Mechanisms, management, and clinical considerations. *Circulation* *133*, 2459–2502.
- Lundgaard, I., Li, B., Xie, L., Kang, H., Sanggaard, S., Haswell, J.D.R., Sun, W., Goldman, S., Blekot, S., Nielsen, M., et al. (2015). Direct neuronal glucose uptake heralds activity-dependent increases in cerebral metabolism. *Nat. Commun.* *6*, 6807.
- Magistretti, P.J., and Allaman, I. (2015). A cellular perspective on brain energy metabolism and functional imaging. *Neuron* *86*, 883–901.
- Mandal, D.K., Bhattacharyya, L., Koenig, S.H., Brown, R.D., 3rd, Oscarson, S., and Brewer, C.F. (1994). Studies of the binding specificity of concanavalin A. Nature of the extended binding site for asparagine-linked carbohydrates. *Biochemistry* *33*, 1157–1162.
- Marvin, J.S., and Hellingna, H.W. (1998). Engineering biosensors by introducing fluorescent allosteric signal transducers: Construction of a novel glucose sensor. *J. Am. Chem. Soc.* *120*, 7–11.
- Marvin, J.S., Schreiter, E.R., Echevarría, I.M., and Looger, L.L. (2011). A genetically encoded, high-signal-to-noise maltose sensor. *Proteins* *79*, 3025–3036.
- Marvin, J.S., Borghuis, B.G., Tian, L., Cichon, J., Harnett, M.T., Akerboom, J., Gordus, A., Renninger, S.L., Chen, T.-W., Bargmann, C.I., et al. (2013). An optimized fluorescent probe for visualizing glutamate neurotransmission. *Nat. Methods* *10*, 162–170.
- Marvin, J.S., Scholl, B., Wilson, D.E., Podgorski, K., Kazempour, A., Müller, J.A., Schoch, S., Quiroz, F.J.U., Rebola, N., Bao, H., et al. (2018). Stability, affinity, and chromatic variants of the glutamate sensor iGluSnFR. *Nat. Methods* *15*, 936–939.
- Marvin, J.S., Shimoda, Y., Magloire, V., Leite, M., Kawashima, T., Jensen, T.P., Kolb, I., Knott, E.L., Novak, O., Podgorski, K., et al. (2019). A genetically encoded fluorescent sensor for in vivo imaging of GABA. *Nat. Methods* *16*, 763–770.
- McCartney, L.J., Pickup, J.C., Rolinski, O.J., and Birch, D.J. (2001). Near-infrared fluorescence lifetime assay for serum glucose based on allophycocyanin-labeled concanavalin A. *Anal. Biochem.* *292*, 216–221.
- Miyamoto, T., and Amrein, H. (2019). Neuronal gluconeogenesis regulates systemic glucose homeostasis in *Drosophila melanogaster*. *Curr. Biol.* *29*, 1263–1272.e5.
- Moses, W.W. (2011). Fundamental limits of spatial resolution in PET. *Nucl. Instrum. Methods Phys. Res. A* *648* (Suppl 1), S236–S240.
- Mueckler, M., Caruso, C., Baldwin, S.A., Panico, M., Blench, I., Morris, H.R., Allard, W.J., Lienhard, G.E., and Lodish, H.F. (1985). Sequence and structure of a human glucose transporter. *Science* *229*, 941–945.
- Nässel, D.R., Kubrak, O.I., Liu, Y., Luo, J., and Lushchak, O.V. (2013). Factors that regulate insulin producing cells and their output in *Drosophila*. *Front. Physiol.* *4*, 252.
- Pellerin, L., and Magistretti, P.J. (1994). Glutamate uptake into astrocytes stimulates aerobic glycolysis: a mechanism coupling neuronal activity to glucose utilization. *Proc. Natl. Acad. Sci. USA* *91*, 10625–10629.
- Pfeiffer, B.D., Truman, J.W., and Rubin, G.M. (2012). Using translational enhancers to increase transgene expression in *Drosophila*. *Proc. Natl. Acad. Sci. USA* *109*, 6626–6631.
- Phelps, M.E., Huang, S.C., Hoffman, E.J., Selin, C., Sokoloff, L., and Kuhl, D.E. (1979). Tomographic measurement of local cerebral glucose metabolic rate in humans with (F-18)2-fluoro-2-deoxy-D-glucose: Validation of method. *Ann. Neurol.* *6*, 371–388.
- Piquet, J., Toussay, X., Hepp, R., Lerchundi, R., Le Douce, J., Favre, É., Guiot, E., Bonvento, G., and Cauli, B. (2018). Supragranular pyramidal cells exhibit early metabolic alterations in the 3xTg-AD mouse model of Alzheimer's disease. *Front. Cell. Neurosci.* *12*, 216.
- Piston, D.W., and Kremers, G.-J. (2007). Fluorescent protein FRET: The good, the bad and the ugly. *Trends Biochem. Sci.* *32*, 407–414.
- Rangaraju, V., Calloway, N., and Ryan, T.A. (2014). Activity-driven local ATP synthesis is required for synaptic function. *Cell* *156*, 825–835.
- Rutter, G.A., Pullen, T.J., Hodson, D.J., and Martinez-Sanchez, A. (2015). Pancreatic  $\beta$ -cell identity, glucose sensing and the control of insulin secretion. *Biochem. J.* *466*, 203–218.
- Schneider, C.A., Rasband, W.S., and Eliceiri, K.W. (2012). NIH Image to ImageJ: 25 years of image analysis. *Nature Methods* *9*, 671–675.
- Schultz, J.S., Mansouri, S., and Goldstein, I.J. (1982). Affinity sensor: A new technique for developing implantable sensors for glucose and other metabolites. *Diabetes Care* *5*, 245–253.
- Skoceck, O., Nöbauer, T., Weiglun, L., Martínez Traub, F., Xia, C.N., Molodtsov, M.I., Grama, A., Yamagata, M., Aharoni, D., Cox, D.D., et al. (2018). High-speed volumetric imaging of neuronal activity in freely moving rodents. *Nat. Methods* *15*, 429–432.
- Soty, M., Gautier-Stein, A., Rajas, F., and Mithieux, G. (2017). Gut-brain glucose signaling in energy homeostasis. *Cell Metab.* *25*, 1231–1242.
- Standaert, M.L., Schimmel, S.D., and Pollet, R.J. (1984). The development of insulin receptors and responses in the differentiating nonfusing muscle cell line BC3H-1. *J. Biol. Chem.* *259*, 2337–2345.
- Studier, F.W. (2005). Protein production by auto-induction in high density shaking cultures. *Protein Expr. Purif.* *41*, 207–234.
- Takanaga, H., Chaudhuri, B., and Frommer, W.B. (2008). GLUT1 and GLUT9 as major contributors to glucose influx in HepG2 cells identified by a high sensitivity intramolecular FRET glucose sensor. *Biochim. Biophys. Acta* *1778*, 1091–1099.
- Takanaga, H., and Frommer, W.B. (2010). Facilitative plasma membrane transporters function during ER transit. *FASEB Journal* *24*, 2849–2858.
- Tian, L., Hires, S.A., Mao, T., Huber, D., Chiappe, M.E., Chalasani, S.H., Petreanu, L., Akerboom, J., McKinney, S.A., Schreiter, E.R., et al. (2009). Imaging neuronal activity in worms, flies and mice with improved GCaMP calcium indicators. *Nat. Methods* *6*, 875–881.
- Tolosa, L., Gryczynski, I., Eichhorn, L.R., Dattelbaum, J.D., Castellano, F.N., Rao, G., and Lakowicz, J.R. (1999). Glucose sensor for low-cost lifetime-based sensing using a genetically engineered protein. *Anal. Biochem.* *267*, 114–120.
- Vaadia, R.D., Li, W., Voleti, V., Singhania, A., Hillman, E.M.C., and Grueber, W.B. (2019). Characterization of proprioceptive system dynamics in behaving *Drosophila* larvae using high-speed volumetric microscopy. *Curr. Biol.* *29*, 935–944.e4.

- Volkenhoff, A., Weiler, A., Letzel, M., Stehling, M., Klämbt, C., and Schirmeier, S. (2015). Glial glycolysis is essential for neuronal survival in *Drosophila*. *Cell Metab.* *22*, 437–447.
- Volkenhoff, A., Hirrlinger, J., Kappel, J.M., Klämbt, C., and Schirmeier, S. (2018). Live imaging using a FRET glucose sensor reveals glucose delivery to all cell types in the *Drosophila* brain. *J. Insect Physiol.* *106*, 55–64.
- Wang, H.-C., and Lee, A.-R. (2015). Recent developments in blood glucose sensors. *Yao Wu Shi Pin Fen Xi* *23*, 191–200.
- Weltin, A., Kieninger, J., and Urban, G.A. (2016). Microfabricated, amperometric, enzyme-based biosensors for in vivo applications. *Anal. Bioanal. Chem.* *408*, 4503–4521.
- Wyatt, G.R., and Kalf, G.F. (1957). The chemistry of insect hemolymph. II. Trehalose and other carbohydrates. *J. Gen. Physiol.* *40*, 833–847.
- Zhu, Q., Wang, L., Dong, Q., Chang, S., Wen, K., Jia, S., Chu, Z., Wang, H., Gao, P., Zhao, H., et al. (2017). FRET-based glucose imaging identifies glucose signalling in response to biotic and abiotic stresses in rice roots. *J. Plant Physiol.* *215*, 65–72.

## STAR★METHODS

### KEY RESOURCES TABLE

REAGENT or RESOURCE	SOURCE	IDENTIFIER
<b>Experimental models: Organisms/strains</b>		
<i>D. melanogaster</i> : w[*] PBac{13XLexAop2-iGlucSnFR-mRuby2}VK00038	Bloomington Drosophila Stock Center	BDSC:82993; FlyBase: FBst0082993
<i>D. melanogaster</i> : P{w[+mC] = tubP-LexA-GAD}1, w[*] PBac{13XLexAop2-iGlucSnFR-mRuby2}VK00038/FM7i, P{w[+mC] = ActGFP}JMR3	Bloomington Drosophila Stock Center	BDSC:82996; FlyBase: FBst0082996
<i>D. melanogaster</i> : P{w[1118]; P{y[+7.7] w[+mC] = GMR57C10-lexA}attP40/CyO}	Bloomington Drosophila Stock Center	BDSC:52817; FlyBase: FBst0052817
Zebrafish: <i>Tg(actb2: iGlucSnFR)</i>	This paper	Plasmid & strain available on request
Zebrafish: <i>Tg(acta1a: jRGECO1a)</i>	This paper	Plasmid & strain available on request
Zebrafish: <i>Tg(actb2: iGlucSnFR; acta1a: jRGECO1a)</i>	This paper	Plasmids available on request
Zebrafish: <i>Tg(actb2: iGlucSnFR; elav/3: jRGECO1a)</i>	This paper	Plasmids available on request
Zebrafish: <i>Tg(fabp10a: iGlucSnFR-mRuby2)</i>	This paper	Plasmid & strain available on request
<i>E. coli</i> : BL21(DE3)pLysS	Thermo-Fisher	C601003
<b>Recombinant DNA</b>		
pAAV. <i>hSynapsin-1</i> .iGlucSnFR-mRuby2	This paper	Addgene: #164510
pAAV. <i>gfABC</i> , <i>D</i> .iGlucSnFR	This paper	Addgene: #164513
pAAV. <i>gfABC</i> , <i>D</i> .iGlucSnFR-mRuby2	This paper	Addgene: #164514
pRSET-A	Thermo-Fisher	V35120
pcDNA3.2/v5-DEST hGlut1	<a href="#">Takanaga and Frommer, 2010</a>	Addgene: #18085
<b>Software and algorithms</b>		
Pro Data SX	Applied Photophysics	<a href="https://www.photophysics.com/support-and-service/documents-and-software/">https://www.photophysics.com/support-and-service/documents-and-software/</a>
Excel	Microsoft	<a href="https://www.microsoft.com/en-us/microsoft-365/excel">https://www.microsoft.com/en-us/microsoft-365/excel</a>
ImageJ	<a href="#">Schneider et al., 2012</a>	<a href="https://imagej.nih.gov/ij/">https://imagej.nih.gov/ij/</a>
ImageJ plug-ins	Jay Unruh, Stowers Institute	<a href="https://research.stowers.org/imagejplugins/">https://research.stowers.org/imagejplugins/</a>
Kaleidagraph	Synergy Software	<a href="https://www.synergy.com">https://www.synergy.com</a>

### RESOURCE AVAILABILITY

#### Lead contact

Requests for information and reagents should be directed to and will be fulfilled by the Lead Contact, Loren L Looger ([loogerl@hhmi.org](mailto:loogerl@hhmi.org)).

#### Materials availability

Plasmids to express iGlucSnFR and iGlucSnFR-mRuby2 in neurons and astrocytes have been deposited at Addgene (Plasmids #164510, 164513, 164514; Key Resources Table). Fly lines expressing iGlucSnFR and iGlucSnFR-mRuby2 are available from the Bloomington *Drosophila* Stock Center (LexAOp2-iGlucSnFR: #82993, LexAOp2-iGlucSnFR-mRuby2: #82996; Key Resources Table). All other unique/stable reagents generated in this study are available from the Lead Contact with a completed Materials Transfer Agreement.

#### Data and code availability

Datasets and code used to analyze the data are available from the Lead Contact.

## EXPERIMENTAL MODEL AND SUBJECT DETAILS

All experimental procedures were carried out in accordance with protocols approved by the HHMI Janelia Research Campus Institutional Animal Care and Use Committee and Institutional Biosafety Committee.

### HEK293 cells

HEK293T cells were obtained from the American Type Culture Collection (CRL-3216). Cells were tested for mycoplasma contamination by the American Type Culture Collection and in-house with the Plasmotest Mycoplasma Assay with HEKBLUE cells. Cells were genetically verified by the Genetic Resources Core Facility at Johns Hopkins University. HEK293T cells were maintained in Dulbecco's modified eagle's medium (DMEM, Life Technologies) supplemented with 10% fetal bovine serum (Corning), at 37°C and 5% CO<sub>2</sub>.

### Flies

*Drosophila melanogaster* of genotypes (LexAop-iGlucSnFR; +; +) and (w/y; 57C10-LexA; +) were used. Flies and larvae were raised on normal cornmeal-molasses fly food at 21.5°C.

### Zebrafish

Adult and larval wild-type zebrafish (WIK strain) were reared at 28.5°C and 14:10 hour light-dark cycle on recirculating life-support systems.

### Rats for generation of cultured neurons and astrocytes

Wild-type Sprague-Dawley rat pups (Charles River) were housed at room temperature in a 12-hour reverse light cycle with food and water *ad libitum*.

## METHOD DETAILS

### Cloning and mutagenesis

The gene for TtGBP, lacking the periplasmic leader sequence, and codon optimized for expression in *E. coli*, was synthesized by PCR assembly from 42 bp fragments and cloned into pRSET-A (Thermo-Fisher) by BamHI/EcoRI digest (with BamHI encoding Gly-Ser). The gene for cpGFP was inserted, with Gly-Gly linkers on either end, between residues 326 and 327 of TtGBP by overlapping PCR. Single and double amino acid mutations were made by the uracil template-based method (Kunkel, 1998).

### Protein purification

Protein was expressed by inoculating 0.5 L auto-induction media plus 100 µg/mL ampicillin with a single *E. coli* BL21(DE3)pLysS bacterial colony transformed with pRSET-A-sensor plasmid and growing overnight at 30°C (Studier, 2005). The growth was then pelleted by centrifugation, resuspended in PBS, and frozen overnight. Cells were lysed by thawing and sonication. Lysate was clarified by centrifugation at 35,000 g and purified by immobilized metal affinity chromatography (IMAC) on a 5 mL Fast Flow Chelating Sepharose column (GE Life Sciences) with an elution gradient from 0 to 200 mM imidazole over 120 mL. Clear fractions with absorbance at 280 nm were pooled, concentrated by spin concentrator, and dialyzed 5x into PBS.

### Stopped-flow fluorescence

Equilibrium binding affinities were determined by titration with serial dilutions of glucose (or decoy molecules) into 100 µL 0.2 µM protein solution in PBS in triplicate using a Tecan Safire plate reading fluorimeter with excitation at 485 nm (5 nm bandpass) and emission at 515 nm (5 nm bandpass). Kinetics of binding were determined by mixing equal volumes of 0.2 µM protein with varying concentrations of glucose in an Applied Photophysics SX20 stopped flow fluorimeter with 490 nm LED excitation and 510 nm long-pass filter. Time courses were fit to a single rising exponential.  $k_1$  and  $k_{-1}$  were determined by plotting  $k_{obs}$  as a function of [glucose] and performing a linear fit assuming a pseudo-first order kinetic mechanism. Kinetic data were fit to a single exponential rise using the Pro Data SX software provided by Applied Photophysics.

### Mutant screening

TtGBP(H66A, H348A)-cpGFP was used as the template for mutagenesis. Mutations were targeted to the Gly-Gly linkers between of TtGBP and cpGFP. Mutated plasmids were transformed into T7 Express cells (New England BioLabs), plated on LB+100 µg/mL ampicillin agar plates and grown overnight at 37°C. Colonies were picked into 2 mL 96-well plates containing 0.9 mL auto-induction media (Studier, 2005) with 100 µg/mL ampicillin and grown overnight with vigorous shaking (400 RPM) at 30°C. Bacterial pellets were collected by centrifugation (3000 g), and resuspended in 0.5 mL PBS by vortexing to wash away endogenous glucose, and pelleted again. The wash procedure was repeated three times, and pellets were frozen overnight at -20°C. Frozen bacterial pellets were then lysed by addition of 1 mL PBS and vortexing. Cellular debris was pelleted by centrifugation and clarified lysate removed for fluorescence assays by pipetting.

The green fluorescence (Ex 485 nm, Em 515 nm, 5 nm bandpass) of 100  $\mu$ L of clarified lysate was measured in a Tecan Safire 2 plate-reading fluorimeter. D-Glucose was added to a final concentration of 10 mM and fluorescence measured again. Variants with increased  $\Delta F/F$  over the starting construct were immediately re-assayed to estimate binding affinity, and winners were streaked out on agar plates, re-isolated, re-assayed, and sequenced. After screening of about 800 variants at each linker, the variant with Linker 1 – PA, Linker 2 – NP was chosen as iGlucoSnFR because it had the highest  $\Delta F/F$ . Fluorescence titrations were fit to a single binding isotherm with Kaleidagraph (Synergy Software).

### Cultured HEK293 cells

Cell culture: Glut1 experiments were done on HEK293 (ATCC #CRL-3216) cells transfected using the Amaxa system (Lonza) and 1  $\mu$ g DNA. Cells were cultured after transfection to densities of 50%–90% confluence in 35 mm coverslip-bottomed culture dishes (MatTek). Cell lines were periodically checked for contamination and genetic identity.

### Cultured neurons/astrocytes

Hippocampi were dissected from P0 neonatal wild-type Sprague-Dawley rat pups (Charles River; housed in a 12-hour reverse light cycle with food and water *ad libitum*) in dissection buffer (500 mL HBSS, 10 mM HEPES, 100 U/mL Penicillin and 10  $\mu$ g/mL Streptomycin (GIBCO 15140-122)), cut into small pieces and dissociated in papain enzyme (Worthington, #PAP2) in dissection buffer for 30 minutes at 37°C. After 30 min of enzyme digestion, papain enzyme solution was removed and tissue pieces dissociated by trituration in MEM (Invitrogen GIBCO 51200-038, no phenol red) with 10% FBS media (500 mL of MEM, 2.5 g D-glucose, 100 mg NaHCO<sub>3</sub>, 50 mg transferrin (Calbiochem 616420), 50 mL FBS (heat inactivated; HyClone SH30071.03 HI), 5 mL 0.2 M L-glutamine solution, 12.5 mg human insulin (Sigma I-6634), 100 U/mL Penicillin and 10  $\mu$ g/mL Streptomycin (GIBCO 15140-122)). Resulting cell suspension was filtered through a 70  $\mu$ m filter to remove remaining pieces of tissue and centrifuged at 90 x g for 7 minutes to pellet. The cell pellet was re-suspended in plating media (500 mL of MEM, 2.5 g D-glucose, 100 mg NaHCO<sub>3</sub>, 50 mg Transferrin, 50 mL FBS, 5 mL 0.2 M L-glutamine solution, 12.5 mg insulin, 100 U/mL Penicillin and 10  $\mu$ g/mL Streptomycin) and counted for cell viability and counts. Cells were plated at 35,000 cells/coverslip with 70  $\mu$ L plating media in the center of a coverslip-bottomed cultured dish (MatTek) and incubated at 37°C for attachment to poly-D-lysine-coated coverslips. After 2+ hours (once cells attached), 1 mL of NbActiv4 media (BrainBits) was added and cultured for two weeks. Media changes were done by removing 0.5 mL and adding 0.5 mL fresh NbActiv4 media. Resulting cultures were infected with AAV viruses one week after plating and were further cultured for 2–3 weeks prior to experiments.

### Perfusion system

A gravity-fed, four-channel perfusion system (VC3-4, ALA Scientific Instruments) was used in all perfusion experiments. The bottoms of the 60 mL feeder syringes were raised to a height which provided flow rates of 4–6 mL/min depending on the fluid level of the syringes. The outlet of the system was directed toward the illuminated area of the coverslip dish at a distance of 1–3 mm, and continuous fast suction at the raised edge of the dish removed solutions. The perfusion outlet was Tygon tubing with 1/16" inner diameter (somewhat larger than that in the manifold), which might have slowed the velocity of the buffers, allowing for less disturbance at the sample. Protocols for buffer switching were carried out by the control software provided. Buffer changes were characterized to be > 90% in 1 s.

### AAVs

AAVs were generated of serotype 2/1 using promoters for neurons (*hSynapsin-1*) or glia (*gfABC<sub>1</sub>D*) and containing either the cytosolic sensor alone (iGlucoSnFR) or the mRuby2-tagged cytosolic sensor (iGlucoSnFR-mRuby2). Viral titers were 1–2  $\times 10^{13}$  GC/mL.

### Flies

Virgin female *Drosophila melanogaster* carrying the intracellularly targeted iGlucoSnFR transgene (LexAop-iGlucoSnFR; +; +) were crossed with males from a driver line (w/y; 57C10-LexA; +) (Pfeiffer et al., 2012) that expresses pan-neuronally in post-embryonic flies. Larvae were raised on normal cornmeal-molasses fly food. Third instar larvae were manually selected, and the CNS was dissected in physiological saline (Lemon et al., 2015). The CNS explants were placed in a 35 mm coverslip-bottom culture dish. To hold the samples stationary, they were partially embedded in a thin layer of 1% low-melting point agarose (SeaPlaque, Lonza) dissolved in physiological saline. After the agarose cooled and polymerized, the embedded CNS explant was then submerged in physiological saline.

### Zebrafish

Adult and larval zebrafish were reared at 28.5°C and 14:10 hour light-dark cycle on recirculating life support systems. Zebrafish were generated using Tol2 transgenesis (Kawakami et al., 2004). Transgenic zebrafish *Tg(actb2: iGlucoSnFR)* express iGlucoSnFR under the  $\beta$ -actin promoter, and hence target nearly all cells. *Tg(acta1a: jRGECO1a)* express the red calcium indicator jRGECO1a in skeletal muscle cells (Higashijima et al., 1997). For liver imaging, the Gateway vector p5E-*fabp10a* was a kind gift from Dr. Michael Pack (University of Pennsylvania); iGlucoSnFR-mRuby2 was cloned in with Gateway cloning. The *fabp10a* construct was co-injected with a *cmc2: eGFP* marker of the heart, to facilitate screening for transgenic lines; no c-injection marker was used for the other lines.

For insulin injection experiments, a non-functional electrophysiological glass patch pipette was mounted on a micromanipulator, and was filled with insulin or blank solutions, along with 1  $\mu\text{M}$  of the red fluorescent dye sulforhodamine 101. This pipette was positioned outside the fish near to the posterior caudal vein prior to the beginning of imaging and a baseline of 5-10 minutes of imaging was collected. Imaging was then paused briefly (10-30 s) while the pipette was inserted. Imaging was immediately restarted, and dye was injected by manual pressure, verified by presence of bright red fluorescence, then the pipette was retracted. When necessary, this pipette was changed to a new pipette containing a different solution, and the procedure repeated in the same imaging session.

### Imaging and image processing: HEK cells

Images of HEK cells co-expressing hGlut1 (Addgene #18085) and iGlucoSnFR-mRuby2 were acquired on an inverted Zeiss LSM 800 confocal microscope equipped with GaAsP detectors and an EC Plan-Neofluar 10x/0.30 M27 objective. Images were 512  $\times$  512 pixels at 16-bit depth, with a frame time of 933 ms. Excitation used laser lines at 488 and 561 nm, with emission ranges of 495-575 and 575-617 nm. The red channel served to confirm that cells were stable during the experiment in the x-y and focal planes but was omitted from further processing. To separate the oscillating component of the signal from gradual baseline drifts or trends, the green (sensor) channel was processed by subtracting a two-sided moving-window average ( $F_{\text{avg}}$ ) corresponding to the period length of the oscillating stimulus, a common de-trending technique. Regions of interest (ROIs) corresponding to co-transfected cells were selected by thresholding an image composed of the oscillation magnitudes at each pixel during the uniform pre-treatment epoch of the experiment, and signals from the detrended data were extracted in these ROIs. Individual ROI traces were then normalized by division by the root mean square deviation (RMSD) of the uniform initial epoch of the experiment and are presented in plots as individual data points. For fitting  $\text{IC}_{50}$ , percent inhibition was calculated as  $100 \cdot [1 - \text{RMSD}_{\text{before}}/\text{RMSD}_{\text{after}}]$  with equal length windows for RMSD calculations.

### Imaging and image processing: neuron/astrocyte co-cultures

Images of hippocampal cultures infected with both AAV2/1-*hSynapsin-1*-iGlucoSnFR-mRuby2 and AAV2/1-*gfaABC<sub>1</sub>D*-iGlucoSnFR or AAV2/1-*hSynapsin-1*-iGlucoSnFR and AAV2/1-*gfaABC<sub>1</sub>D*-iGlucoSnFR-mRuby2 were acquired on an inverted Zeiss LSM 800 confocal microscope equipped with GaAsP detectors and an EC Plan-Neofluar 20x/0.80 M27 objective. Images were 1024  $\times$  512 pixels at 16-bit depth, with a frame time of 933 ms. Excitation used laser lines at 488 and 561 nm, with emission ranges of 495-575 and 575-617 nm. The red channel served to differentiate cell types. Images were processed by first average-binning over time by a factor of two, followed by detrending to separate the oscillating component ( $\Delta F$ ) of the signal from gradual baseline drifts or trends ( $F_{\text{avg}}$ ). The experimental green (sensor) channel was processed by subtracting  $F_{\text{avg}}$  from the original image stack, yielding  $\Delta F$ , then divided by  $F_{\text{avg}}$ , yielding a  $\Delta F/F_{\text{avg}}$  image stack. Regions of interest (ROIs) over mRuby2-expressing cells were selected by thresholding the red channel  $F_{\text{avg}}$  image stack using a reasonably low (mean) threshold, converting to a binary mask, then minimum-projected to identify regions that were consistently fluorescent in the red channel over the course of the experiment. The green  $F_{\text{avg}}$  stack was then multiplied by this mask and minimum-projected, then thresholded by maximum entropy to identify remaining fluorescent green ROIs. ROIs greater than 50 pixels in size were identified, and mean intensities under these ROIs were evaluated in the green channel  $\Delta F/F_{\text{avg}}$  image stack. These traces were then averaged and presented. The somewhat complex nature of this processing procedure was designed in the hopes of identifying and differentiating with highest certainty cells expressing iGlucoSnFR and not iGlucoSnFR-mRuby2 and that were consistently fluorescent over the course of the experiment (a few cells disappeared, detached, or moved).

To identify cells that expressed iGlucoSnFR-mRuby2 and not iGlucoSnFR, the  $F_{\text{avg}}$  stack in the red channel was thresholded using the “moments” threshold in FIJI/ImageJ, followed by minimum projection and identification of ROIs which were consistent fluorescent in the red channel. These ROIs were then evaluated in green channel  $\Delta F/F_{\text{avg}}$  stack and presented.

The exact same processing procedure was used in both types of experiments: AAV2/1-*hSynapsin-1*-iGlucoSnFR-mRuby2 with AAV2/1-*gfaABC<sub>1</sub>D*-iGlucoSnFR or AAV2/1-*hSynapsin-1*-iGlucoSnFR and AAV2/1-*gfaABC<sub>1</sub>D*-iGlucoSnFR-mRuby2.

Raw, time-averaged, mean intensity values in the green channel of all ROIs were measured as well, and no obvious correlation of intensity with oscillation magnitudes was observed.

### Imaging and image processing: *Drosophila* CNS

Images of explanted 3<sup>rd</sup> instar CNS expressing iGlucoSnFR-mRuby2 pan-neuronally (*57C10* driver) were acquired on an inverted Zeiss LSM 800 confocal microscope equipped with GaAsP detectors and an EC Plan-Neofluar 20x/0.8 M27 objective. Data were collected as 8  $\times$  5  $\mu\text{m}$  planes at 1024  $\times$  512 pixels at 16-bit depth, with a volume rate of  $\sim$ 9 s. Excitation used laser lines at 488 and 561 nm, with emission ranges of 505-550 and 565-650 nm. The red channel, which remained roughly stable in intensity over the course of the experiment, served to confirm the glucose specificity of signal as well as allow for ratiometric imaging, which was found to be unnecessary. The same moving-window subtraction detrending process described above was used to accentuate oscillations and drew attention to the rostral-caudal glucose increase pattern described. Pixelwise temporal FFT analysis allowed plotting of the graded phase shifts along the rostral-caudal axis.

### Imaging and image processing: Zebrafish larvae

For data on muscle, imaging was carried out as described above. To extract signals in the spontaneous twitch experiments, image stacks were first registered over time by the green channel. ROIs were then identified by first normalizing local contrast in the image stack and thresholding. These ROIs were tracked over time in the original raw image stacks, and mean fluorescence intensities in each ROI in both green and red channels were quantified, then averaged together and plotted. For both insulin and epinephrine data, images were first registered in the green channel, then a simple rectangular ROI was selected for simplicity of presentation. In the epinephrine experiments, there was some deformation of the subject upon addition of epinephrine, complicating presentation of a “clean” still image displaying fluorescence changes. A rectangular ROI (35 pixels x 225 pixels) was selected based on relative structural stability of the region as well as fluorescence intensity changes. Neighboring regions in XYZ were confirmed not to manifest opposing/mirrored responses (which would suggest that the observed signal was a motion artifact).

### QUANTIFICATION AND STATISTICAL ANALYSIS

The only statistical test used is the Mann-Whitney test between the all-neurons and all-astrocytes groups in Figure S3; the test was calculated in Microsoft Excel. Statistical details of experiments (including exact value of n, what n represents, the definition of center, and dispersion) are given in the figure legends, and are consolidated here as well:

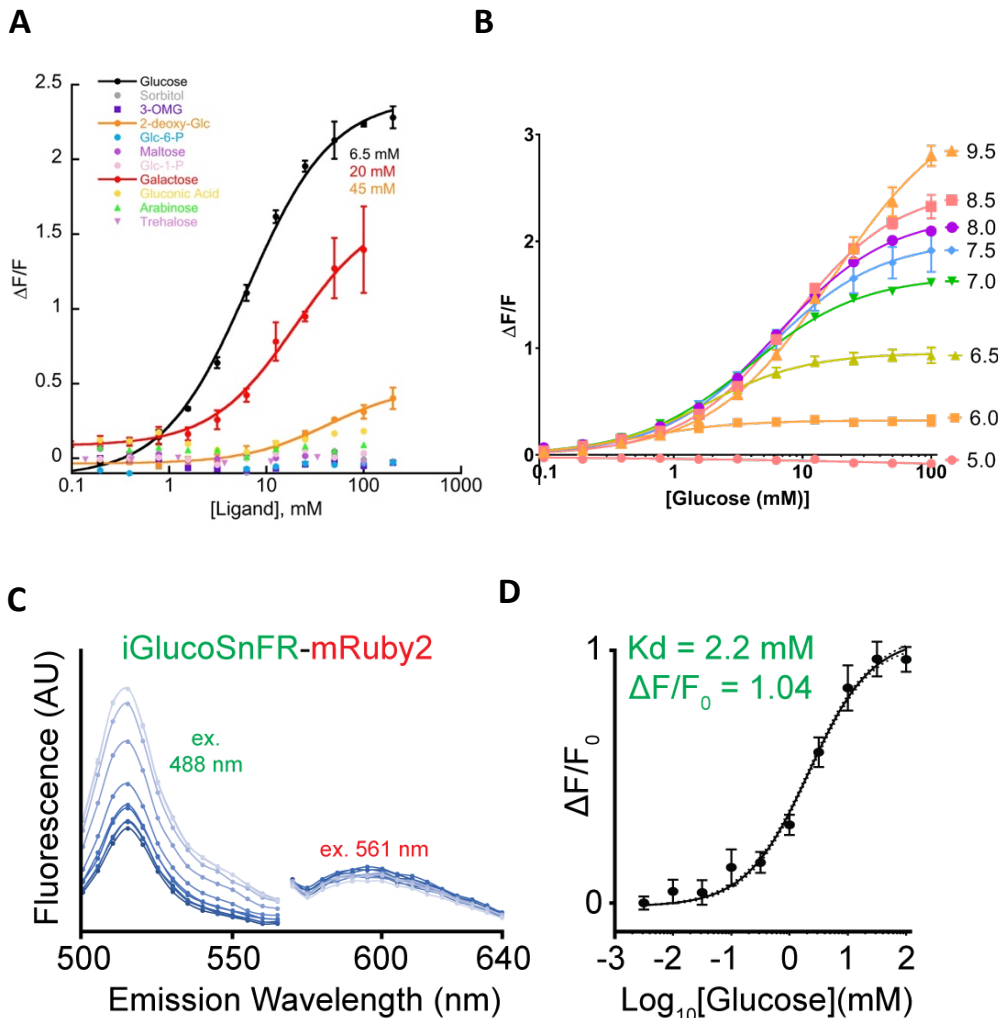
- Figure 1D: n = 3 experimental replicates (separate dilutions of single protein preparation with glucose titrations), mean, std. dev.
- Figure 1E: n = 3 experimental replicates (separate dilutions of single protein preparation with glucose titrations), mean, std. dev.
- Figure 1F: n = 5 experimental replicates (separate dilutions of single protein preparation with glucose addition to specified concentration in stopped-flow apparatus), mean, std. dev.
- Figure 1G: n = 3 experimental replicates (separate dilutions of single protein preparation with glucose titrations), mean, std. dev.
- Figure 2G: n = 61 segmented astrocyte ROIs and n = 55 segmented neuron ROIs, mean, std. dev.
- Figure 3D: n = 7,875 pixels within 35 × 225 pixel rectangular ROI, mean, std. dev.
- Figure S1A: n = 3 experimental replicates (separate dilutions of single protein preparation with ligand titrations), mean, std. dev.
- Figure S1B: n = 4 experimental replicates (separate dilutions of single protein preparation with glucose titrations per pH point), mean, std. dev.
- Figure S1D: For each value of [glucose] for each titration, 4 technical replicates were performed at each of 5 wavelengths.  $\Delta F/F$  was calculated for each, and these 20 values were averaged to produce the mean for that titration. The titration was performed 3 times with separate dilutions from a single protein preparation and ligand titration – the mean of the values for the 3 titrations was plotted, as well as the std. dev. of those 3 values. The curve fit shows a fit to the Hill equation using the  $3 \times 4 \times 5 = 60$  titrations.

Cell Reports, Volume 35

**Supplemental information**

***In vivo* glucose imaging in multiple  
model organisms with an engineered  
single-wavelength sensor**

**Jacob P. Keller, Jonathan S. Marvin, Haluk Lacin, William C. Lemon, Jamién Shea, Soomin Kim, Richard T. Lee, Minoru Koyama, Philipp J. Keller, and Loren L. Looger**

**Figure S1****Figure S1. In vitro characterization of iGlucoSnFR. Related to Figure 1.**

**(A).** Titration of glucose and decoy ligands. Glucose bound most tightly, with a  $K_d$  of  $6.5 \pm 0.4 \text{ mM}$ , and only galactose and 2-deoxy-glucose showed any fluorescence changes ( $K_d$ 's =  $20 \pm 3$  and  $45 \pm 7 \text{ mM}$ , respectively). 3-OMG is 3-O-methyl-glucose, Glc-6-P is glucose-6-phosphate, Glc-1-P is glucose-1-phosphate. All titrations performed in PBS at  $25^\circ\text{C}$ . Traces are mean of  $n=3$  experimental replicates; error bars are std. dev. **(B).** iGlucoSnFR pH dependence. iGlucoSnFR was titrated over a range of pH values, revealing a pH dependence both of  $K_d$  and  $\Delta F/F$ , with larger pH values tending to increase both. Traces are mean of  $n=4$  experimental replicates; error bars are std. dev. **(C).** Fluorescence spectra of mRuby2-tagged iGlucoSnFR. iGlucoSnFR tagged with mRuby2 in the same polypeptide was expressed in *E. coli* and purified. Emission spectra in the green emission band at various glucose concentrations were indistinguishable from the green-only sensor. Red emission spectra were unresponsive to glucose and were indistinguishable from mRuby2. **(D).** iGlucoSnFR responses to glucose in the green emission band were somewhat different from those in the green-only sensor. As mentioned in the main text, this construct was difficult to purify to homogeneity when expressed bacterially, so it is hard to be confident in the accuracy of these titrations, especially in light of the cellular data showing identical responses to identical stimuli. Overall  $n = 60$ : 3 replicate titrations were measured 4 times each at 5 wavelengths on

the green peak.  $\Delta F/F$  for each titration, measurement, and wavelength, were calculated first, then fit by the Hill equations as 60 titrations. Error bars represent mean and standard deviation.

## Figure S2

>iGlucoSnFR

MGDRSKLEIFSWWAGDEGPALALIRLYKQKYPGVEVINATVTGGAGVNARAVLKTRMLGGDPPDTFQVH  
AGMELIGTWVVANRMEDLSALFRQEGWLQAFPKGLIDLISYKGGIWSVPVNIHRSNVMWYLPKCLKWGV  
NPPRTWDEFLATCQTLKQKGLEAPLALGENWTQOHLWESVALAVLGPDDWNNLWNGKLFKFTDPKAVRAWE  
VFGRVLDCAKDAAGLSWQQAVDRVVQGAAFNVMGDWAAGYMTTTLKLPKPGTDFAWAPSPGTQGVFMMML  
SDSFGLPKGAKNRQAINWLRLVGSKEGQDTFNPLKGSIAARLSDPSKY**PASHNVYIMADKQKNGIKAN**  
**FKIRHNIEDGGVQLAYHYQONTPIGDGPVLLPDNHYLSTQSKLSKDPNEKRDHMLLEFVTAAGITLGM**  
**ELYKGGTGGSMVSKGEELFTGVVPIVLVDGDVNGHKFSVSGEGEGDATYGKLTTLKFICTTGKLPVPWPT**  
**LVTTLTYGVQCFSRYPDHMKQHDFFKSAMPEGYIQERTIFFKDDGNYKTRAEVKFEGDTLVNRIELKID**  
**FKEDGNILGHKLEYNFN****NP****NAYGQSAMRDWRSNRIVGSLVHGAVAPESFMSQFGTVMEIFLQTRNPQAAA**  
**NAAQAIADQVGLGRLGQLQVDEQKLISEEDLNAVQDTQERFYCENEVGS.**

TtGBP, Linker, cpGFP, Myc tag, ER export motif

>iGlucoSnFR-mRuby2

MGDRSKLEIFSWWAGDEGPALALIRLYKQKYPGVEVINATVTGGAGVNARAVLKTRMLGGDPPDTFQVH  
AGMELIGTWVVANRMEDLSALFRQEGWLQAFPKGLIDLISYKGGIWSVPVNIHRSNVMWYLPKCLKWGV  
NPPRTWDEFLATCQTLKQKGLEAPLALGENWTQOHLWESVALAVLGPDDWNNLWNGKLFKFTDPKAVRAWE  
VFGRVLDCAKDAAGLSWQQAVDRVVQGAAFNVMGDWAAGYMTTTLKLPKPGTDFAWAPSPGTQGVFMMML  
SDSFGLPKGAKNRQAINWLRLVGSKEGQDTFNPLKGSIAARLSDPSKY**PASHNVYIMADKQKNGIKAN**  
**FKIRHNIEDGGVQLAYHYQONTPIGDGPVLLPDNHYLSTQSKLSKDPNEKRDHMLLEFVTAAGITLGM**  
**ELYKGGTGGSMVSKGEELFTGVVPIVLVDGDVNGHKFSVSGEGEGDATYGKLTTLKFICTTGKLPVPWPT**  
**LVTTLTYGVQCFSRYPDHMKQHDFFKSAMPEGYIQERTIFFKDDGNYKTRAEVKFEGDTLVNRIELKID**  
**FKEDGNILGHKLEYNFN****NP****NAYGQSAMRDWRSNRIVGSLVHGAVAPESFMSQFGTVMEIFLQTRNPQAAA**  
**NAAQAIADQVGLGRLGQLQVDEQKLISEEDLNAVQDTQERMVSKGEELIKENMRMKVMEGVSNGHQFK**  
**CTGEGGNPYMGTQTMRIKVIIEGGPLPFAFDILATSFMYGSRTFIKYPKGIPTDFKQSFPEGFTWERVTR**  
**YEDGGVVTVMQDTSLEDGCLVYHVQVRGVNFPNGPVMQKKTGWEPNTEMMYPADGGLRGYTHMALKVD**  
**GGHLSCSFVTTYRSKKTVGNIKMPGIHAVDHRLEERLEESDNEMFVVQREHAVAKFAGLGGGMDELYKFY**  
**CENEVGS.**

TtGBP, Linker, cpGFP, Myc tag, mRuby2, ER export motif

Figure S2. Amino acid sequence of iGlucoSnFR and iGlucoSnFR-mRuby2. Related to Figure 1. Colored by motifs as indicated.

Figure S3

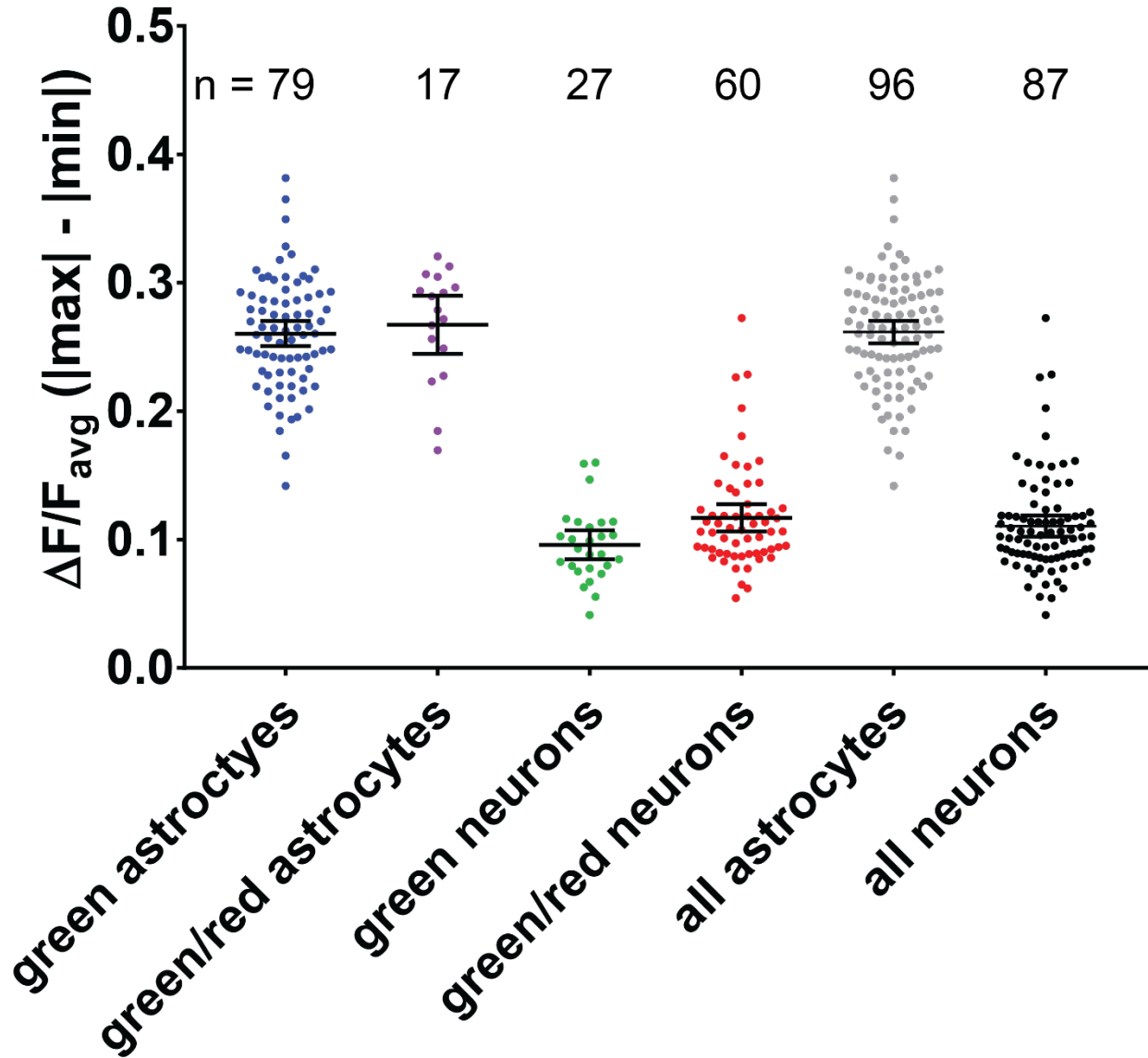


Figure S3. Astrocyte/neuron experiments with iGlucSnFR and/or iGlucSnFR-mRuby2. Related to Figure 2. Astrocyte/neuron co-cultures were infected with either the combination (AAV2/1-*hSynapsin1*-iGlucSnFR and AAV2/1-*gfaABC1D*-iGlucSnFR-mRuby2), which yielded green neurons and green/red astrocytes, or (AAV2/1-*hSynapsin1*-iGlucSnFR-mRuby2 and AAV2/1-*gfaABC1D*-iGlucSnFR), which yielded green/red neurons and green astrocytes. Responses were imaged and quantified identically in both cases and showed that the presence or absence of the tag did not change the observed magnitudes of oscillation. The difference between all-astrocytes and all-neurons was significant ( $p < 10^{-16}$ , Mann-Whitney test). All data points (corresponding to cells/ROIs) are shown, along with mean and 95% confidence intervals.

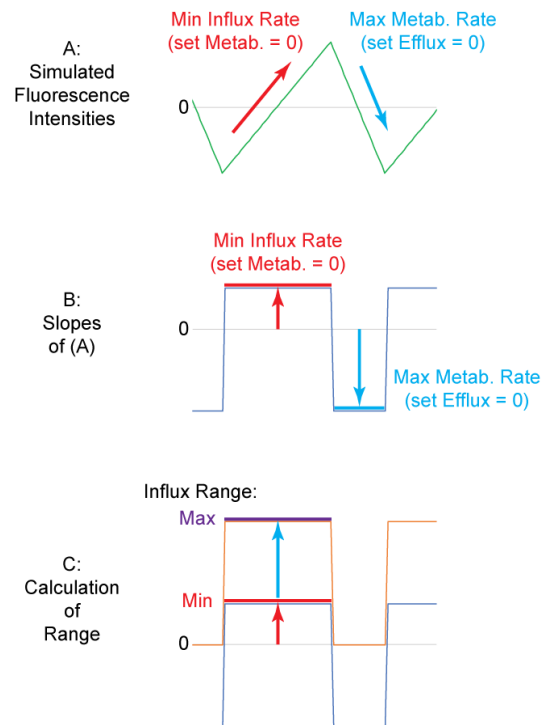
## Methods S1: Semi-quantitative disentanglement of glucose transport and metabolism *via* OSTA waveform analysis. Related to Figure 2.

Calibration of intracellular biosensors *in situ* remains challenging. For one thing, whatever means are used to control cytosolic conditions (*e.g.*, permeabilization with detergents, porins, or ionophores) will inherently perturb the physiological state in multiple ways. Using glucose transport and metabolism in neuron-astrocyte co-cultures, we here outline a “semi-quantitative” approach to the problem.

In attempting to measure glucose transport in neuron-astrocyte co-cultures or other living cells, however, a further experimental complication is layered on top of the calibration issue. Metabolic consumption of glucose becomes intertwined with transport phenomena, leading to underestimates of uptake and overestimates of efflux. Since the true metabolic consumption rate of each cell is not known, it is essentially impossible to determine the true underlying transport rates, even with ideal calibration. What can be determined trivially and unambiguously, however, are the maximum and minimum influx rates given the observed rates of fluorescence, which will give an idea of the relative transport rates of cellular sub-populations. This, namely putting upper and lower bounds on the transport rates, is what is meant by “semi-quantitative” above.

There are a few properties of astrocytes and neurons that should be noted in assessing glucose

dynamics. First, glucose transporters in astrocytes (Glut1) and neurons (Glut3) are passive uniporters whose properties are well known: as passive transporters, their transport rates will be governed only by the glucose gradients across them, and concentrative effects are not possible. Therefore, intracellular glucose concentrations will not exceed extracellular concentrations. Second, under given conditions, rates of glucose metabolism will be governed by the concentration of intracellular glucose according to enzyme kinetics, regardless of whether concentrations are rising or falling. Applying these assumptions to OSTA-type data, it can be inferred that the upper bound of metabolic rate is represented by the downward slope in the downstrokes of the assay (**Methods SubFigure 1A**, blue arrows). In reality, this downward slope includes a transporter-mediated efflux component as well, but the limiting case would be when none of this negative slope is attributable to efflux. Since this upper bound for metabolic rate is now known, it can be extrapolated to the upstrokes, since each glucose concentration in the downstroke has an analogous point in the upstroke at which the metabolic rates will be equal. In the case of linear or near-linear “sawtooth” waveforms as

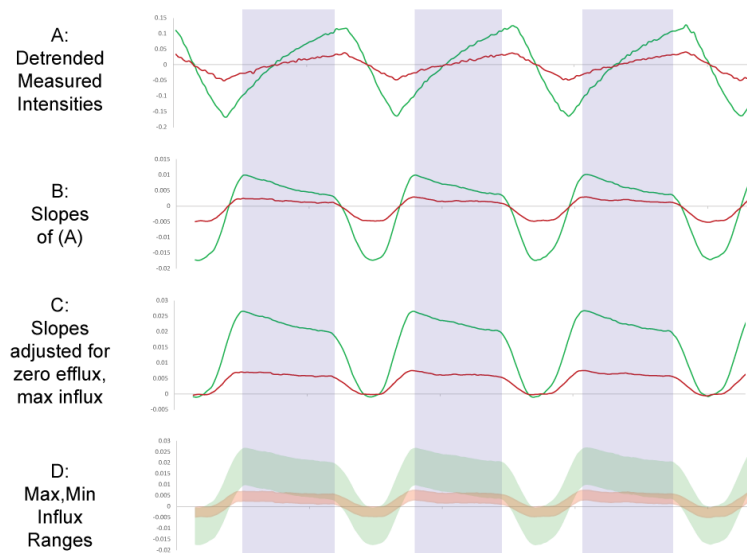


Methods SubFigure 1: Theory

in the current data, this calculation simplifies to subtracting the constant negative slope (maximum metabolic rate) from the slopes across the entire waveform, yielding a maximum rate for influx in the upstrokes. In this way, under given conditions, a maximum bound for influx rate can also be inferred.

The lower bound for influx rate can be also be derived by supposing the metabolic rate to be zero, and attributing the measured fluorescence increase in the upstroke to transport, undiminished by metabolic consumption. This lower bound is therefore simply the measured slope in the upstrokes (**Methods Figure 1A**, red arrows). These lower and upper bounds define a range of possible influx rates given the observed intensity changes, and when the ranges of two cell populations in a given field of view are compared, a semi-quantitative idea of their relative transport rates can be achieved.

When this procedure is applied to experimental astrocyte-neuron co-culture data (**Methods SubFigure 2**), the following results are obtained. While a cursory examination of the experimental traces indicates ~3-fold higher transport rates in astrocytes versus neurons, it may be argued that metabolism plays a significant role, and is greater in neurons than in astrocytes. Neuronal transport rates would then be underestimated. Using the semi-quantitative procedure described above, ranges can be derived, showing that the minimum possible influx rate of astrocytes is still larger than the maximum possible influx rate in neurons.



Methods SubFigure 2: Application of theory to data

This may not, however, be the end of the story: another possibility to consider is that neurons might have a high level of resting glucose, such that the sensor is more saturated and actual neuronal glucose changes are underestimated by fluorescence changes relative to those measured in astrocytes. This cannot be the case, however, since the glucose transporters in the system are passive, such that the cytosolic glucose concentrations cannot be greater than the maximum extracellular concentrations (20 mM), at which point the response of the sensor is still approximately linear (the sensor  $K_d$  is ~5 mM). Even more compellingly, since the fluorescence traces oscillate stably at certain levels, the only factor that would influence tonic glucose levels would be metabolic rate. And this effect would tend to work in the opposite direction: higher metabolic rates would lead to lower tonic glucose, which in turn would tend to increase the observed magnitude of the oscillations. Accordingly, even assuming maximal glucose consumption rates in neurons (which would tend to decrease tonic glucose and increase sensor response magnitudes) and minimal consumption rates in astrocytes, the two populations are still markedly different, with astrocytes having larger glucose transport rates.

The conclusions above can be drawn directly from the current data. If, however, these results are interpreted in light of published measurements of astrocytic and neuronal metabolic rates, which show 1-2-fold greater metabolic rates in astrocytes versus neurons (Bittner, C. X., et. al. High resolution measurement of the glycolytic rate. *Frontiers in Neuroenergetics*. <https://doi.org/10.3389/fnene.2010.00026> (2010)), the difference in the populations becomes even

greater, and the factor of ~3-fold greater transport in astrocytes mentioned above is likely an underestimate.

Nevertheless, there remains a possibility that the sensor's properties vary across different cell types, leading to different responses to equivalent glucose levels. The most likely candidate would be differences in cytosolic pH differences, which are known to affect the response of the sensor (**Figure S1B**), but published measurements reveal almost identical cytosolic pH in cultured astrocytes and neurons under similar conditions (Verkhatsky, A., Nedergaard, M. Physiology of astroglia. *Physiol. Rev.* **98**, 239-389 (2018)). Concentrations of other ions ( $K^+$ ,  $Na^+$ ,  $Ca^{2+}$ ,  $Mg^{2+}$ ,  $Cl^-$ ) are also similar. There may be other unknown factors perturbing sensor properties, but the above combination of data-centered reasoning and published measurements of cytological properties of cultured neurons and astrocytes support the conclusion that astrocytes in culture uptake glucose faster than neurons under identical conditions.